JFM PAPERS

Global dynamics and topology of two-phase mixing layer flow through simultaneous gas and liquid velocity measurements

Alessandro Della Pia[1,2,†], Theodoros Michelis[3], Matteo Chiatto[2], Marios Kotsonis[3] and Luigi de Luca[2]

[1]Scuola Superiore Meridionale, School for Advanced Studies, Naples 80138, Italy

[2]Department of Industrial Engineering, University of Naples 'Federico II', Naples 80125, Italy

[3]Section of Aerodynamics, Delft University of Technology, Delft 2629HS, The Netherlands

This study reports the first time-resolved particle image velocimetry characterization of a planar two-phase mixing layer flow, whose velocity field is measured simultaneously in gas and liquid streams. Two parallel air and water flows meet downstream of a splitter plate, giving rise to an initially spanwise invariant configuration. The aim is to elucidate further the mechanisms leading to the flow breakup in gas-assisted atomization. The complete experimental characterization of the velocity field represents a database that could be used in data-driven reduced-order models to investigate the global behaviour of the flow system. After the analysis of a selected reference case, a parametric study of the flow behaviour is performed by varying the liquid (Re_l) and gas (Re_g) Reynolds numbers, and as a consequence also the gas-to-liquid dynamic pressure ratio (M), shedding light on both time-averaged (mean) and unsteady velocity fields. In the reference case, it is shown that the mean flow exhibits a wake region just downstream of the splitter plate, followed by the development of a mixing layer. By increasing both Re_l and Re_g, the streamwise extent of the wake decreases and eventually vanishes, the flow resulting in a pure mixing layer regime. The spectral analysis of the normal-to-flow velocity fluctuations outlines different flow regimes by variation of the governing parameters, giving more insights into the global characteristics of the flow field. As a major result, it is found that at high Re_g and M values, the velocity fluctuations are characterized by low-frequency temporal oscillations synchronized in several locations within the flow field, which suggest the presence of a global mode of instability. The proper orthogonal decomposition of velocity fluctuations, performed in both gas and liquid phases, reveals finally that the synchronized oscillations are associated with a low-frequency dominant flapping mode of the gas–liquid interface. Higher-order modes correspond to interfacial wave structures travelling with the so-called

† Email address for correspondence: alessandro.dellapia@unina.it

Dimotakis velocity. For lower gas Reynolds numbers, the leading modes describe higher frequency fingers shedding at the interface.

Key words: gas/liquid flow, shear waves

---

1. Introduction

Investigations of the physical mechanisms determining the interfacial instability in gas–liquid mixing layer flows date back to two centuries ago (Helmholtz 1868). Typical industrial configurations where this kind of two-phase flow can be encountered are the air-blast atomizers, such as liquid fuel injectors in combustion engines. In these applications, a relatively low-speed liquid jet interacts with a faster parallel co-flowing gaseous phase downstream of a separator (or splitter) plate, which initially separates the fluids (Raynal *et al.* 1997; Ben Rayana, Cartellier & Hopfinger 2006; Eggers & Villermaux 2008). The velocity difference existing between the two phases triggers a shear instability at the separating interface, leading to the generation of waves in the liquid phase, which are in turn affected by secondary instabilities, determining the formation, corrugation and finally breaking of liquid ligaments into droplets (primary atomization). This process leads to the generation of mutually interacting gas–droplets mixtures, in the so-called secondary atomization, i.e. the last stage of an 'instability cascade' (Marmottant & Villermaux 2004). Among others, the application of such a flow configuration to fuel injection is a topic of primary interest for both automotive and aerospace industrial sectors. The quality of combustion and then pollutant generation in fuel injection depend crucially on the characteristics of the liquid phase atomization (Lefebvre 1989). For these reasons, the understanding and modelling of such a process have been leading scientific research through extensive theoretical, experimental and numerical investigations for decades. However, a comprehensive understanding of the physical mechanisms governing the different stages of the instability cascade is yet to be obtained, making the modelling and control of two-phase mixing layer flows still challenging tasks nowadays.

The present study focuses on the early stages of the primary instability of the gas–liquid interface, and it aims to investigate the salient features of mixing layer flow that establishes just downstream of the splitter plate. The elucidation of the flow dynamics in the near field region is of critical importance, due to its impact on the downstream turbulent flow field development (Ling *et al.* 2019). From a theoretical point of view, the dynamics of the interfacial waves developing in proximity of the splitter plate edge has been investigated in the literature usually through linear stability analysis. Through superposition of small perturbations to a proper time-invariant base flow, within the parallel (or quasi-parallel) flow approximation, the general aim is to determine the most unstable frequency and wavelength of the interfacial instability.

First investigations were carried out assuming an inviscid regime for both the base flow and the evolution of perturbations (Marmottant & Villermaux 2004; Eggers & Villermaux 2008). Later, Matas, Marty & Cartellier (2011) observed that the inclusion of a velocity deficit in the base flow, to mimic the splitter plate effect on the near-field flow region, is crucial to obtain reasonable quantitative agreement between inviscid stability analysis predictions and experimental measurements of the interface oscillations frequency, although the spatial growth rate was significantly underestimated with this approach.

A good quantitative match between measured and theoretically predicted spatial growth rates of the interfacial wave was obtained through the inclusion of viscous effects in the temporal linear stability analysis, i.e. by formulating an Orr–Sommerfeld problem for the two-phase shear layer (Boeck & Zaleski 2005; Yecko, Zaleski & Fullana 2005); however, predictions of the interfacial oscillations frequency resulted in overestimates. To obtain a more satisfactory and systematic agreement between stability analysis predictions and experimental measurements, Otto, Rossi & Boeck (2013) developed a local spatio-temporal linear stability approach, improving the theoretical–experimental match for both frequency and spatial growth rate. Moreover, their method provided for the first time evidence of a transition from convective to absolute instability for the injection conditions reported in the work by Matas *et al.* (2011), with experimental data spanning both instability regimes. This aspect was clarified further by Fuster *et al.* (2013), who showed that the transition from convective to absolute flow behaviour depends crucially on the dynamic pressure ratio parameter (M).

More recently, Matas (2015) found that the absolute instability can also be triggered by a confinement effect, consisting in the finite thicknesses of gas (H_g) and liquid (H_l) streams at the injection. By means of linear stability analysis, Matas, Delon & Cartellier (2018) highlighted that the confinement instability is related to a resonance mechanism taking place between normal-to-flow velocity perturbations within the gaseous phase, which are induced by the streamwise liquid waves development, and the gas injector size (H_g).

The survey of past works summarized above points out that one of the most challenging aims to enhance the agreement between linear stability predictions and experimental measurements of the two-phase mixing layer flow behaviour is an accurate knowledge of the selected base flow. Numerical simulations performed in both three-dimensional (Agbaglah, Chiodi & Desjardins 2017; Ling *et al.* 2017, 2019) and two-dimensional (Fuster *et al.* 2013; Bozonnet *et al.* 2022) scenarios have shown that the two-phase mixing layer is characterized by strong spatial variations in the near-field region, where the flow field can be considered two-dimensional (i.e. invariant along the span of the splitter plate). The locally parallel flow assumption usually made for linear stability calculations is thus generally not accurate. As pointed out by Bozonnet *et al.* (2022), a global stability analysis should be performed on linear and/or nonlinear mean flows to improve the capability to predict the flow dynamics in most of the experimental conditions.

The two-phase mean flow characterization of such a mixing layer configuration, and in general of free surface flows in the presence of a wavy interface, poses severe challenges from an experimental point of view (Kosiwczuk *et al.* 2005; Sanchis & Jensen 2011; Ayati *et al.* 2014; Andrè & Bardet 2015; Buckley & Veron 2017). In most cases, when studying interfacial phenomena through particle image velocimetry (PIV) or particle tracking velocimetry (PTV), the illuminating light sheet is oriented perpendicular to the interface, eventually causing undesirable reflections in the form of bright spots. Dynamic masking techniques can be used to detect the interface in such cases, as done in Sanchis & Jensen (2011) by applying the Radon transform algorithm to PIV images of a stratified air–water flow in a circular pipe, obtaining also the velocity field within the liquid phase.

The large difference in refractive index between phases can also lead to glare and prevent optical access. Particular care must be taken to ensure that the flow tracers do not modify the liquid properties, such as surface tension and viscosity. Finally, the large disparity in the two phases injection velocities (about two orders of magnitude in mixing layer configurations of practical interest, where the liquid stream is slower) makes the simultaneous PIV characterization of the two phases a severe issue when using a single-laser single-camera measuring configuration.

Combined PIV and laser-induced fluorescence have been used recently to perform the interface detection and mean flow measurements in the gaseous phase over wind driven surface waves (Buckley & Veron 2017), while both phases of a stratified air–water flow in a horizontal pipe (Ayati *et al.* 2014) and a turbulent spray mixture (Kosiwczuk *et al.* 2005) have been characterized by means of sophisticated multi-camera (Kosiwczuk *et al.* 2005; Ayati *et al.* 2014) and multi-laser (Buckley & Veron 2017) instrumentation. Measurements by PIV of the mean gaseous velocity field have also been performed by Descamps, Matas & Cartellier (2008) for a planar air–water mixing layer configuration.

It is noteworthy that despite the strong spatial and temporal dynamics coupling between the two phases, previous investigations have so far eluded simultaneous velocity measurements. Therefore, as an important step to assist future global stability studies, the major objective of this work is to provide a detailed experimental characterization of the planar air–water mixing flow developing downstream of a splitter plate, which initially separates the two gaseous and liquid streams. The present measurements constitute a database that could be used in data-driven reduced order models to investigate the global behaviour of the flow system. Linear and nonlinear approaches have been proposed recently, as documented for example by Colanera, Della Pia & Chiatto (2022), for the case of vertical liquid jets in still air, and Li *et al.* (2021), who introduced the cluster-based network models to reproduce the dynamics of a system by means of a directed network of nodes. The transition properties between the nodes are based on high-order direct transition probabilities identified from the data. In the configuration studied here, such an analysis could be performed on experimental snapshots.

By means of carefully arranged light sheet optics, two-component time-resolved particle image velocimetry (TR-PIV) measurements are performed simultaneously in air and water streams, employing a single-laser single-camera set-up. The adopted measurement configuration allows one to acquire instantaneous snapshots of the two phases, which are then separated by post-processing.

The two-phase mean (time-averaged) and unsteady features of the flow are characterized for several injection conditions, providing to the authors' knowledge the first simultaneous TR-PIV measurements of a planar mixing layer in gas and liquid phases. The mean flow is analysed in terms of detailed velocity profiles and overall portraits, first focusing on a selected reference case. A parametric study of the mean flow topology is then performed by varying the liquid (Re_l) and gas (Re_g) Reynolds numbers, and as a consequence also the gas-to-liquid dynamic pressure ratio (M). Finally, physical insights on the unsteady flow characteristics are gained through the spectral analysis and proper orthogonal decomposition (POD) of velocity fluctuations, discussed through comparisons with previous findings in the literature.

2. Flow configuration and methodology

The set-up realized to perform air–water mixing layer experiments (inspired by the previous works of Raynal *et al.* 1997; Ben Rayana *et al.* 2006; Matas *et al.* 2011) is presented first (§ 2.1), followed by a description of the PIV measurement technique employed to characterize the two-phase flow (§ 2.2).

2.1. *Experimental set-up*

A schematic representation of the experimental apparatus is shown in figure 1. Figure 1(*a*) gives an overview of all the main components, including the measurement set-up
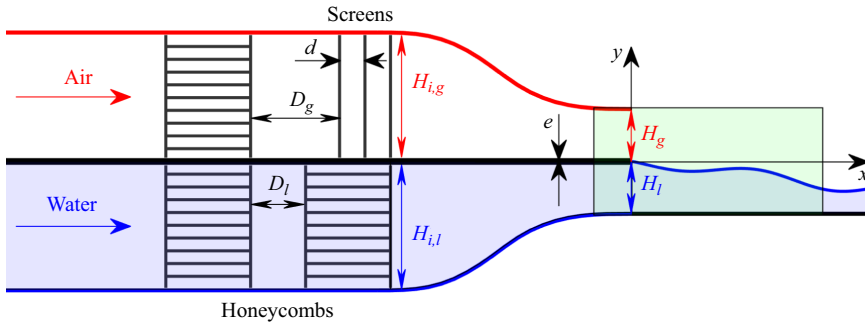
(*a*)
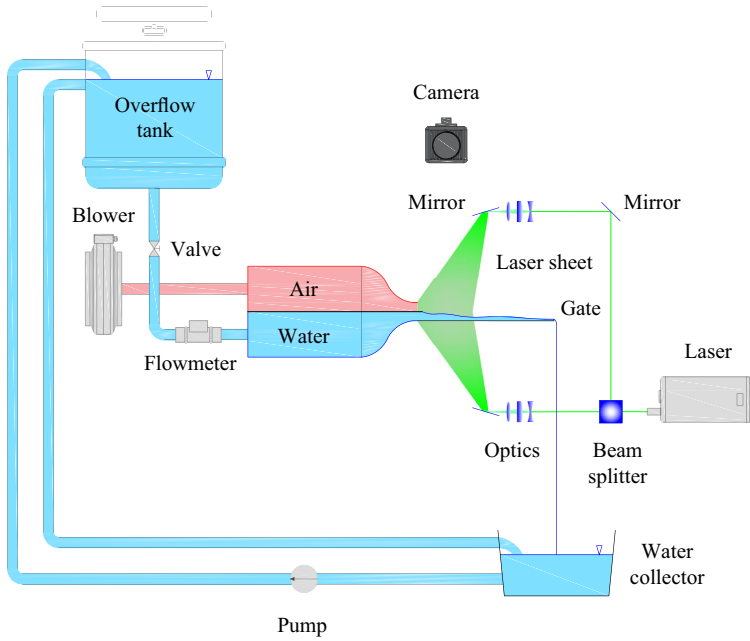
(*b*)

Figure 1. (*a*) Overall schematic representation and (*b*) two-dimensional sketch close to the nozzle exit section of the experimental set-up. In (*b*), the PIV measurement region of interest is highlighted in green.

(discussed later, in § 2.2), while figure 1(*b*) focuses on the near-field flow region of the mixing layer, i.e. immediately after the nozzle exit section, which is located at $x = 0$. A water stream flows along the streamwise direction (x) below a parallel faster air stream, the two fluids being separated initially by a stainless steel splitter plate with thickness $e = 2$ mm (figure 1*b*). The shapes of the water and air channels are the same. The walls are made from Plexiglas, with cross-sectional area (in the yz plane) initially 100 mm × 100 mm (where y and z are the normal-to-flow and spanwise coordinates, respectively). Then a two-dimensional converging nozzle reduces the channel height from 100 mm to $H_g = H_l = 20$ mm at $x = 0$ (see table 1), where the flows issue into a test section. Three-dimensional effects due to the lateral confinement of the test section walls on the liquid jet are negligible in the near-field region of the flow, where the two-dimensional PIV measurements are realized.

Name	Variable	Value	Unit
Gas nozzle inlet height	$H_{i,g}$	100	mm
Gas nozzle outlet height	H_g	20	mm
Honeycomb-to-screen distance in gas	D_g	50	mm
Screen-to-screen distance in gas	d	20	mm
Liquid nozzle inlet height	$H_{i,l}$	100	mm
Liquid nozzle outlet height	H_l	20	mm
Honeycomb-to-honeycomb distance in liquid	D_l	30	mm
Splitter plate thickness	e	2	mm

Table 1. Relevant geometrical quantities of the experimental set-up (see also figure 1*b*).

An overflow tank (figure 1*a*) positioned 1.5 m above the splitter plate drives the liquid flow by gravity, and is filled up continuously by a pump (T.I.P. TVX 12 000 Dompelpomp), thus realizing a closed-loop circuit for the water stream. At the end of the test section, the liquid flow spills out into a water collector. The flow rate, which is kept constant during each experiment, is regulated by means of a valve located upstream of the water channel entry; different values measured by a LVB-25-A vortex flowmeter are obtained, corresponding to liquid inlet velocities in the range $U_l \in [0.10, 0.30]$ m s^{-1}. For each liquid flow rate value, the height of the water stream at the splitter plate edge (i.e. at $x = 0$) is kept constant (equal to H_l) by adjusting the height of a gate placed at the end of the test section ($x = 500$ mm), before the liquid is dispensed into a collector. In this way, air ingestion into the water channel at the splitter plate edge is avoided for all the testing conditions.

The air stream is generated by a blowing machine (Rück Ventilatoren RS315LEC) allowing us to obtain injection velocities in the range $U_g \in [2, 15]$ m s^{-1}, as measured by a Pitot tube located at the gas nozzle exit section midpoint (i.e. at $x = 0$, $y = 10$ mm), and cross-checked by static pressure probes positioned at the inlet ($x = -250$ mm) and outlet ($x = 0$) sections of the convergent nozzle. Flow conditioners are used in both the liquid and gas channels to damp velocity fluctuations; two aluminum honeycombs (aluNID from Alucoat) with 50 mm long hexagonal cells are employed in the liquid phase, while a combination of the same honeycomb and mesh screens is used in the air channel.

Particular care is taken in designing the flow conditioners for the gas phase to control its turbulence intensity level, which has been shown to affect the mixing layer development in both experimental (Matas *et al.* 2015) and numerical (Jiang & Ling 2020, 2021) studies, and that depends strongly on screen geometrical properties and relative streamwise spacing in a multiple screens configuration (see, for example, the works by Mehta & Bradshaw 1979; Marshall 1985; Groth & Johansson 1988). Following Groth & Johansson (1988), we chose a combination of metal meshes (figure 1*b*), with mesh size decreasing progressively from 1 mm (coarse screen) to 0.5 mm (fine), and constant relative spacing $d = 20$ mm, while a distance $D_g = 50$ mm was selected between the honeycomb and the first (i.e. located more upstream) coarse screen (see table 1). This configuration gives a turbulence intensity level below 1 % for all the testing conditions, as reported in figure 2(*a*). The turbulence intensity is quantified in terms of root mean square (rms) of the gas velocity fluctuation $u'(t) = u(t) - \bar{u}$, where $u(t)$ is the streamwise velocity component measured (in absence of liquid stream) by a hot wire located at the gas nozzle exit section midpoint, and $\bar{u}$ its time-averaged value. Note that the values of the gas turbulence intensity reported here are close to the lowest value ($u'_{rms}/\bar{u} = 0.8$ %) found by Matas *et al.* (2015) in
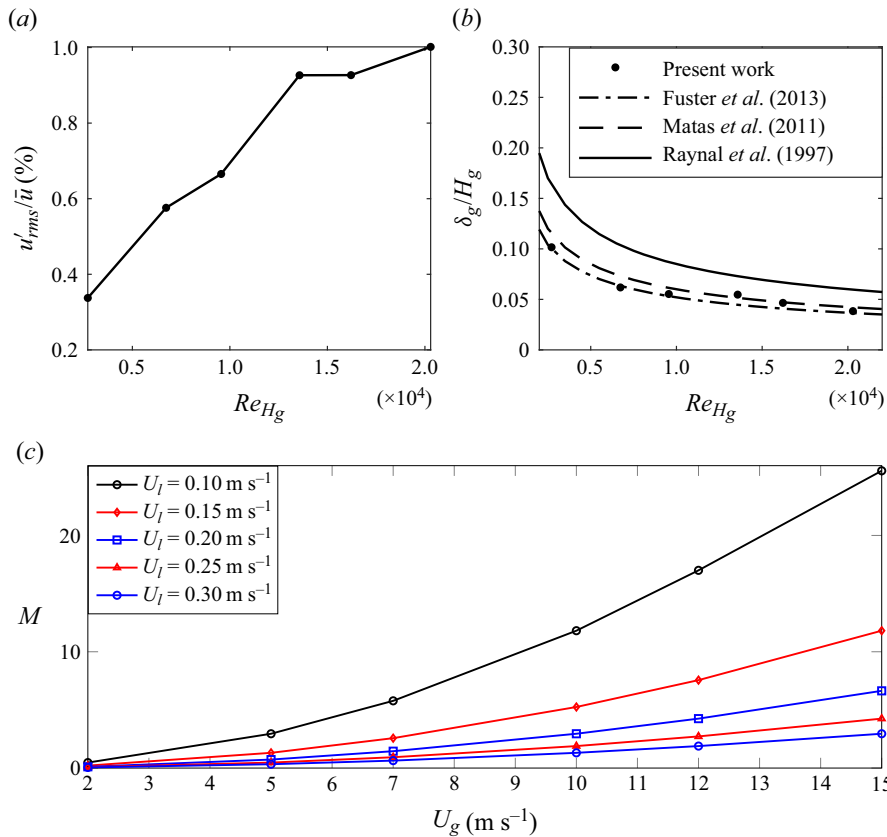
Figure 2. (*a*) Air flow turbulence intensity level $u'_{rms}/\bar{u}$, and (*b*) inlet gas vorticity thickness δ_g, varying with gas Reynolds number Re_{H_g}. Comparisons with past works are also reported in (*b*). (*c*) An overview of the testing conditions in terms of dynamic pressure ratio M values as a function of the gas velocity U_g at different liquid velocities U_l.

their experimental analysis of the gas turbulence effect on the dynamics of an air–water mixing layer. Moreover, Matas *et al.* (2015) found that the peak frequency of the air–water interface oscillations was influenced by the gas turbulence only for values $u'_{rms}/\bar{u} > 3.5\,\%$. Therefore, we can assert that results reported in the present work are not influenced by the turbulence intensity level of the gaseous phase.

Reynolds number values reported in figure 2(*a*) correspond to $U_g = 2, 5, 7, 10, 12,$ 15 m s^{-1}, the Reynolds number here being defined as $Re_{H_g} = \rho_g U_g H_g / \mu_g$, where ρ_g and μ_g are respectively the gas density and dynamic viscosity. The inlet gas vorticity thickness δ_g, which is defined as $\delta_g = \Delta\bar{u}/(\mathrm{d}\bar{u}/\mathrm{d}y)|_{max}$ ($\Delta\bar{u} = \bar{u}(y = H_g/2) - \bar{u}(y = e/2)$) and is known to play a crucial role in the mixing layer instability selection mechanisms (Matas *et al.* 2011; Fuster *et al.* 2013), has also been measured by positioning the hot wire at a downstream distance $x = e/2$. The obtained values are reported in figure 2(*b*) as a function of Re_{H_g}, revealing a good agreement with the scaling law $\delta_g/H_g = 5.2/\sqrt{Re_{H_g}}$ proposed by Fuster *et al.* (2013). An overview of the testing conditions considered in this work is summarized in figure 2(*c*), where liquid and gas injection velocities are reported together with the corresponding dynamic pressure ratio $M = \rho_g U_g^2/(\rho_l U_l^2)$ values.

2.2. *Measurement technique*

The single-laser single-camera measurement system designed to achieve the TR-PIV characterization of the flow simultaneously in the two phases is shown schematically in figure 1(*a*). As discussed in the Introduction, performing this type of measurement is challenging, and other strategies such as combining PIV with laser-induced fluorescence (Buckley & Veron 2017) or employing multi-camera multi-laser configurations (Kosiwczuk *et al.* 2005; Ayati *et al.* 2014) have been explored to date. The major issues are related to the laser light reflection and refraction across the interface, and to the high velocity difference between the two phases (about two orders of magnitude).

In the present work, to enlighten simultaneously air and water flows overcoming light reflections at the interface, a Continuum Mesa PIV 532-120M laser operated at 2 kHz double pulse rate (pulse energy 18 mJ) is used to generate a light beam, which is then separated into two beams by a prism. The first beam goes through a combination of two spherical and one cylindrical lenses and a mirror, thus becoming a thin sheet enlightening the liquid phase. The second beam is rotated horizontally by a mirror, and is transformed into an analogous sheet for the air flow by the same combination of lenses and mirror. A high-speed (2 kHz repetition rate in double exposure mode) camera (Photron, Fastcam SA-1, 1024 × 1024 pixels), whose axis is orthogonal to the laser sheets plane, and a programmable timing unit (LaVision, HSC, not shown in figure 1), complete the measurement set-up. Atomized droplets (mean diameter 1 µm) are seeded in the air channel by a fog generator (SAFEX, Fog 2010+) using a working fluid of water–glycol mixture, while a 20 µm polyamide Vestosint powder is used to seed the liquid phase.

A field of view $[-18, 108] \times [-21, 21]\,\text{mm}^2$ (shown qualitatively in green in figure 1*b*) is imaged by mounting a 105 mm objective (Nikon, Micro-Nikkor) on the high-speed camera, thus giving a two-dimensional region of interest within the *xy* plane positioned midway from the channel side walls. By adjusting the camera focus, particle images approximately 2–3 px in diameter are obtained in both liquid and gas phases, as shown in the raw image reported in figure 3(*a*). An algorithm written in MATLAB is used to pre-process the raw images (figure 3*b*) and separate air and water phases (figures 3*c,d*), which are then post-processed separately through LaVision DaVis 10. An iterative multi-grid cross-correlation scheme with window deformation (Scarano & Riethmuller 2000) is used to compute velocity fields, and results are post-processed with the universal outlier detection algorithm (Westerweel & Scarano 2005). The time delay between two successive frames in air is adjusted from $\Delta t_g = 200\,\mu\text{s}$ to $\Delta t_g = 70\,\mu\text{s}$ for $U_g \in [2, 15]\,\text{m s}^{-1}$, while values ranging from $\Delta t_l = 10.5\,\text{ms}$ to $\Delta t_l = 1.2\,\text{ms}$ are employed for cross-correlation in water ($U_l \in [0.10, 0.30]\,\text{m s}^{-1}$), to guarantee a peak particle displacement of approximately 10 pixels in both phases. For each pair of U_g and U_l values, the time delay Δt_l for cross-correlation in water is adjusted simply by skipping the number of frames necessary to achieve the same peak particle displacement as in air, i.e. $U_l\,\Delta t_l = U_g\,\Delta t_g$. In the final pass of the cross-correlation operation, the interrogation window size and the overlapping ratio are 16 px × 16 px and 50 %, respectively, leading to spatial resolution 1 mm per vector. Mean quantities are estimated based on $N_t = 8000$ realizations, with average measurement uncertainty on the streamwise and normal-to-flow velocity components respectively in the ranges [0.62, 9.43] % and [0.71, 6.28] % of the injection velocities (increasing value moving towards walls).

The PIV measurements allow us to complement the air stream characterization in terms of inflow conditions as shown in figure 4. In particular, the mean streamwise velocity component profile $\bar{u}$ is shown at three different streamwise stations upstream of the injection section: $x/H_g = -1$ (figure 4*a*), $x/H_g = -0.5$ (figure 4*b*) and $x/H_g = -0.1$

(*a*)

(*b*)

(*c*)   (*d*)
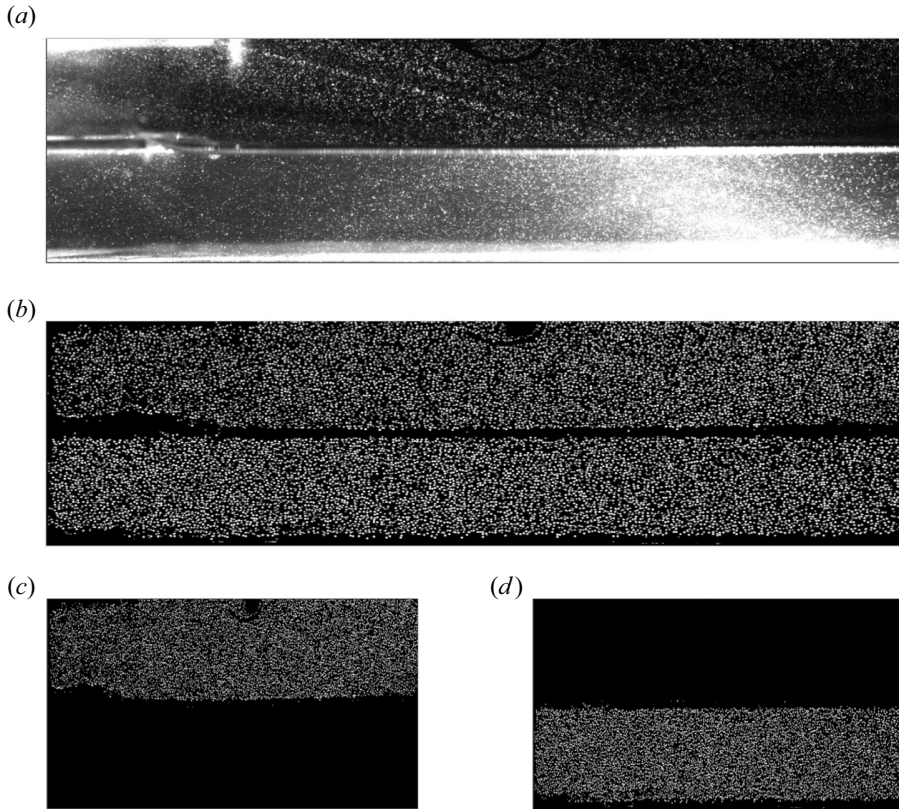

Figure 3. Single-laser single-camera PIV measurement workflow: (*a*) acquired raw image, (*b*) pre-processing, and (*c*,*d*) phase separations.
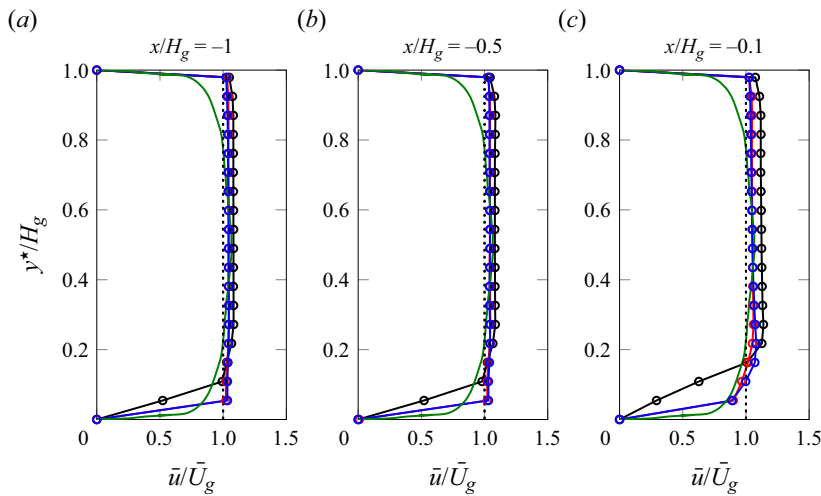

Figure 4. Velocity profile in air at different streamwise stations upstream of the injection section by varying the Reynolds number: $Re_{H_g} = 6.7 \times 10^3$ (black curves), $Re_{H_g} = 9.6 \times 10^3$ (red curves), $Re_{H_g} = 16.2 \times 10^3$ (blue curves). The numerical solution of the fully developed turbulent channel flow obtained by Kim, Moin & Moser (1987) at Reynolds number 13 750 is also reported for comparison (green curve).

(figure 4c). Note that the normal-to-flow coordinate y has been shifted by $e/2$ ($y^\star = y - e/2$), such that $\bar{u} = 0$ at $y^\star = 0$, and $\bar{U}_g$ denotes the mean velocity at each station. Three velocity profiles are reported in each panel, corresponding to $Re_{H_g} = 6.7 \times 10^3$ (black curves), 9.6×10^3 (red curves) and 16.2×10^3 (blue curves), and the numerical solution of the fully developed turbulent channel flow obtained by Kim *et al.* (1987) at Reynolds number 13 750 is also reported for comparison (green curve). The velocity profile tends to the fully developed turbulent channel flow solution as Re_g increases, thus highlighting a transition towards turbulent inflow conditions. This occurrence seems to be confirmed by the trend of the turbulence intensity reported in figure 2(*a*), showing an initially increasing behaviour followed by a plateau. Of course, each velocity profile is not symmetric with respect to the y direction, due to the intrinsic shape of the exit nozzle, limited by the flat splitter plate and the converging lateral wall (where the boundary layer is thinner).

3. Mean flow analysis

The mean flow topology is discussed first for a selected case, which has been defined as the REF case and is characterized by values of flow quantities reported in table 2. Later, the effect of injection conditions on the two-phase flow field is investigated by means of a parametric analysis involving the dimensionless numbers

$$Re_l = \frac{\rho_l U_l \delta_l}{\mu_l}, \quad Re_g = \frac{\rho_g U_g \delta_g}{\mu_g}, \quad M = \frac{\rho_g U_g^2}{\rho_l U_l^2}, \quad (3.1a\text{–}c)$$

whose values are reported in table 3 for the main cases considered in the analysis. The inlet liquid vorticity thickness δ_l, which is defined analogously to δ_g and is obtained from the PIV measured velocity profiles in water, is used to define the liquid Reynolds number Re_l, which varies from 302 (L1 case) to 807 (L3 case). The gas Reynolds number Re_g, based on the gas vorticity thickness δ_g, varies from 384 (G1 case) to 768 (G5 case). We note explicitly that the three dimensionless numbers defined in (3.1a–c) are not all independent of each other: for example, one can vary Re_g by fixing Re_l, but as a consequence, the third parameter M also varies. Note also that as the ratio e/δ_g is greater than unity for all the cases examined (last row of table 3), the present investigation lies within the so-called injector-influenced regime outlined by Fuster *et al.* (2013).

3.1. *The REF case*

The time-averaged velocity magnitude $\bar{V}$ contour is shown in figure 5(*a*) together with the velocity vectors distribution, and a zoom around the splitter plate immediately downstream of the nozzle exit section is provided in figure 5(*b*). For all cases discussed within this work, the mean quantities $\bar{u}$ and $\bar{v}$ are computed over a total of 8000 temporal realizations of the flow.

Note that in figure 5, the velocity magnitude has been scaled with respect to U_g, the spatial coordinates have been made dimensionless by means of the splitter plate thickness, i.e. $\tilde{x} = x/e$ and $\tilde{y} = y/e$, and the time-averaged interface location has been represented as a white dashed line. Moreover, here as elsewhere, velocity vectors in the liquid phase have been magnified by a factor of $O(10^2)$.

After issuing from the injection section ($\tilde{x} = 0$), the air and water flows meet downstream of the splitter plate. By moving along the streamwise direction, two distinct

Name	Variable	Value	Unit
Gas density	ρ_g	1.177	kg m^{-3}
Liquid density	ρ_l	997	kg m^{-3}
Gas viscosity	μ_g	1.84×10^{-5}	kg m^{-1} s^{-1}
Liquid viscosity	μ_l	8.90×10^{-4}	kg m^{-1} s^{-1}
Surface tension coefficient	σ	72.5×10^{-3}	N m^{-1}
Inlet liquid velocity	U_l	0.15	m s^{-1}
Inlet gas velocity	U_g	7	m s^{-1}
Inlet gas vorticity thickness	δ_g	1.1×10^{-3}	m
Inlet liquid vorticity thickness	δ_l	2.7×10^{-3}	m
Splitter plate thickness	e	2.0×10^{-3}	m

Table 2. Dimensional quantities corresponding to the REF case.

Case name	REF	L1	L2	L3	G1	G2	G3	G4	G5
Re_l	454	302	515	807	454	454	454	454	302
Re_g	493	493	493	493	384	704	714	768	768
M	2.57	5.78	1.45	0.64	1.31	5.25	7.56	11.81	25.56
e/δ_g	1.81	1.81	1.81	1.81	1.62	1.83	2.15	2.60	2.60

Table 3. Overview of the main cases considered in the analysis. The dimensionless parameters Re_l, Re_g and M are defined by (3.1*a–c*).
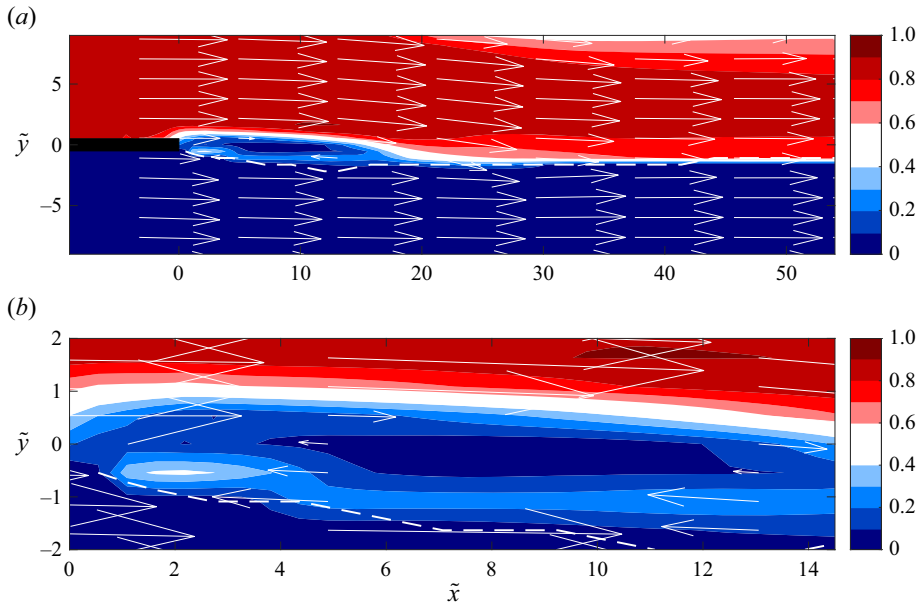
Figure 5. (*a*) Time-averaged velocity magnitude $\bar{V}/U_g$ contour, with (*b*) zoom next to the nozzle exit section. The splitter plate is highlighted in black, the time-averaged interface location is represented as a white dashed line, and velocity vectors are also reported. REF case of table 3.
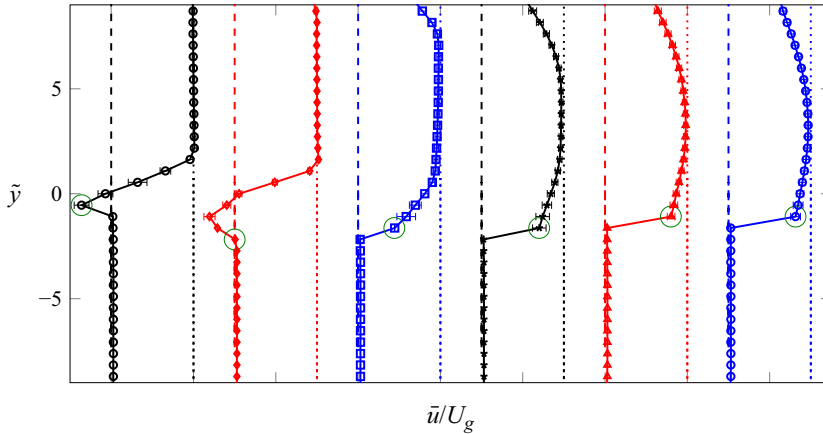
Figure 6. Time-averaged streamwise $\bar{u}(\tilde{y})/U_g$ velocity component profiles at different $\tilde{x}$ stations: 0.55 (black circles), 10.88 (red diamonds), 21.76 (blue squares), 32.10 (black stars), 42.98 (red triangles), 53.31 (blue circles). The dashed and dotted lines represent the values $\bar{u}/U_g = 0$ and 1, respectively, and error bars denote the average measurement uncertainty, while green circles highlight the interface location. REF case of table 3.

regions can be detected: a wake $(0 < \tilde{x} < \tilde{x}_w)$ and a pure mixing layer $(\tilde{x} > \tilde{x}_w)$ region, with $\tilde{x}_w = x_w/e = 17.5$. The wake region length $\tilde{x}_w$ has been calculated as the last streamwise station (starting from $\tilde{x} = 0$) where $\bar{u}(\tilde{y}) < 0$ (i.e. $\bar{u} > 0$ for $\tilde{x} > \tilde{x}_w$). The spatial development of the mixing layer is more clearly quantified in figure 6, which reports $\bar{u}(\tilde{y})$ profiles at different streamwise stations spanning both air and water streams, together with the corresponding average measurement uncertainty. The reverse flow component within the wake region is highlighted by the negative values of $\bar{u}$ for $\tilde{y}$ around zero. Far from $\tilde{y} = 0$, the velocity profile is characterized by an almost uniform distribution in both air $(\tilde{y} > 2)$ and water $(\tilde{y} < -1.1)$ streams, while it undergoes strong spatial variations within the region $-1.1 < \tilde{y} < 2$. Downstream of the wake region, the velocity profile is influenced by the air–air mixing layer forming between the injected gas stream and the external still ambient, with consequent reduction of the local $\bar{u}$ value by increasing $\tilde{y}$ (phenomenon of jet expansion; see Descamps *et al.* 2008).

By moving along $\tilde{x}$, the momentum exchange between the faster gas and the slower water stream leads to the progressive reduction of the velocity deficit, which is the difference between the minimum and the free-stream local liquid velocities $(\bar{u}_{min} - U_l)$. This aspect is clarified in figure 7, which shows the velocity profile at three selected downstream stations, respectively inside $(\tilde{x} = 0.55$, black curve), just outside $(\tilde{x} = 20.13$, red curve) and far from $(\tilde{x} = 53.31$, blue curve) the wake region (figures 7a,b), and the velocity deficit streamwise distribution (figure 7c), together with the corresponding average measurement uncertainty.

The different regions characterizing the flow topology are further highlighted by $\bar{u}(\tilde{x})$ and $\bar{v}(\tilde{x})$ velocity profiles, shown respectively in figures 8(a,b), for normal-to-flow stations spanning both air and water streams. The distribution $\bar{u}(\tilde{x}, \tilde{y} = 0)$ highlights the strong spatial variation characterizing the flow field in the wake region (blue curve in figure 8a), while $\bar{v}(\tilde{x})$ profiles reveal the downward deviation of the gas stream (i.e. negative values of $\bar{v}(\tilde{x})$) in the near-field region, as a result of the combination of water jet contraction (Agbaglah *et al.* 2017) and air recirculation within the wake.

Figures 9 and 10 show the Reynolds stress tensor components $\overline{u'u'}$, $\overline{v'v'}$ and $\overline{u'v'}$ in terms of contour representations and $\tilde{y}$ profiles, respectively. The $\tilde{x}$ velocity component fluctuation is evaluated as $u' = u - \bar{u}$, and the same applies for v'. The $\overline{u'u'}(\tilde{y})$ distribution
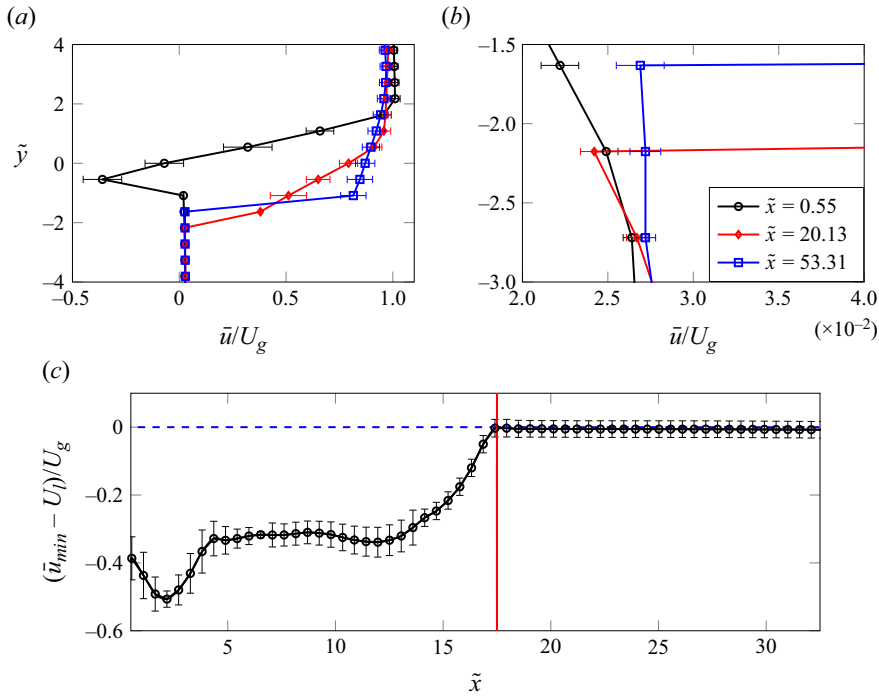
981 A13-12

Figure 7. (*a*) Time-averaged streamwise $\bar{u}(\tilde{y})/U_g$ velocity component profiles at different $\tilde{x}$ stations, with (*b*) zoom near the liquid phase, and (*c*) velocity deficit $(\bar{u}_{min} - U_l)/U_g$ streamwise distribution. In (*c*), the vertical red line denotes the wake region length $\tilde{x}_w$, the horizontal blue dashed line denotes the zero, and error bars represent the average measurement uncertainty. REF case of table 3.

(figures 9*a* and 10*a*) is characterized by larger peaks than the others (figures 9*b*,*c* and 10*b*,*c*), as also found by Ling *et al.* (2019) by means of three-dimensional direct numerical simulations. Moreover, all the distributions are peaked in correspondence with the maximum momentum exchange locations, namely at the air–water and air–air mixing layers (the latter on the image top), as already evidenced in discussing figure 6 (see also Jiang & Ling 2021). Similarly, the streamwise $\overline{u'u'}(\tilde{x})$ distribution reported in figure 10(*d*) reveals two peaks, the first immediately downstream of the splitter plate, and the second at $\tilde{x}_w = 17.5$, namely at the end of the recirculation region. It is also possible to appreciate that for each $\tilde{y}$ location, a constant value is approached asymptotically as $\tilde{x}$ increases, revealing that the mixing layer progressively achieves a self-similar state moving far from the wake region (Mehta 1991).

The analysis of the REF case is concluded by reporting a comparison between the measured velocity profiles and the theoretical base flows proposed by Otto *et al.* (2013) and Fuster *et al.* (2013) in the context of the local stability analysis. The comparison is performed at two distinct streamwise stations: the first inside the wake region ($\tilde{x} < \widetilde{x_w}$, figures 11*a*,*b*), and the second just outside it ($\tilde{x} > \widetilde{x_w}$, figures 11*c*,*d*). Note that the measured profiles (black curves) have been represented by employing the shifted coordinate $y^\star$, defined previously in § 2.2, to facilitate the comparisons with theoretical formulae (red curves) provided hereafter.
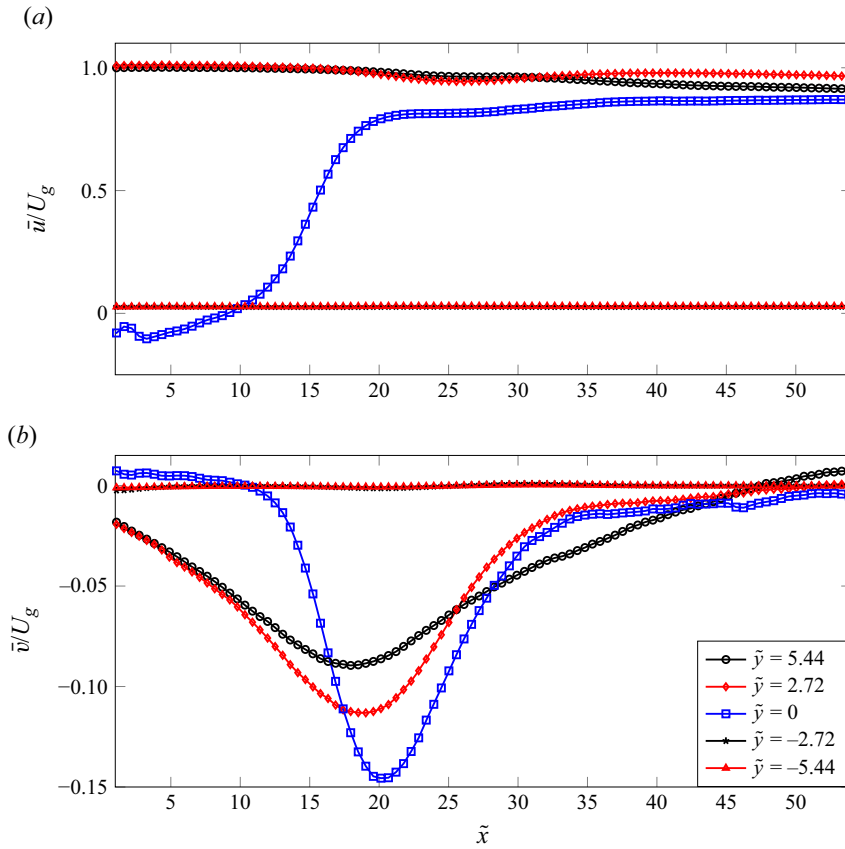
981 A13-13

(*a*)

(*b*)

Figure 8. (*a*) Time-averaged streamwise $\bar{u}(\tilde{x})/U_g$ and (*b*) normal-to-flow $\bar{v}(\tilde{x})/U_g$ velocity component profiles at different $\tilde{y}$ stations. REF case of table 3.

The analytical velocity profile used in figures 11(*c*,*d*) reads as

$$\frac{u^+}{U_m} = \begin{cases} -\dfrac{U_l}{U_m}\operatorname{erf}\left(\dfrac{y^\star}{\delta_l}\right) + \dfrac{\bar{u}_0}{U_m}\left[1 + \operatorname{erf}\left(\dfrac{y^\star}{\delta_d}\right)\right], & y^\star \leq 0, \\[4mm] \dfrac{U_g}{U_m}\operatorname{erf}\left(\dfrac{y^\star}{\delta_g}\right) + \dfrac{\bar{u}_0}{U_m}\left[1 - \operatorname{erf}\left(\dfrac{y^\star}{\delta_d}\right)\right], & y^\star \geq 0, \end{cases} \tag{3.2}$$

which is the same as that reported by Fuster *et al.* (2013) once small notational differences are rectified, while a modified version (discontinuous at $y^\star = 0$) is adopted for comparisons in the wake region (figures 11*a*,*b*),

$$\frac{u^-}{U_m} = \begin{cases} -\dfrac{U_l}{U_m}\operatorname{erf}\left(\dfrac{y^\star}{\delta_l}\right) + \dfrac{\bar{u}_0}{U_m}\left[1 + \operatorname{erf}\left(\dfrac{y^\star}{\delta_d}\right)\right], & y^\star \leq 0, \\[4mm] \dfrac{U_g}{U_m}\operatorname{erf}\left(\dfrac{y^\star - y^\star_{min}}{\delta_g}\right) + \dfrac{\bar{u}_{min}}{U_m}\left[1 - \operatorname{erf}\left(\dfrac{y^\star - y^\star_{min}}{\delta_d}\right)\right], & y^\star > 0. \end{cases} \tag{3.3}$$

In (3.2)–(3.3), the error function $\operatorname{erf}(y^\star)$ is employed, $U_m = (U_g + U_l)/2$, $\bar{u}_0$ is the measured velocity at the air–water interface (an analytical estimation based on continuity of shear stresses across the interface was used by Fuster *et al.* 2013), $\bar{u}_{min}$ is the minimum
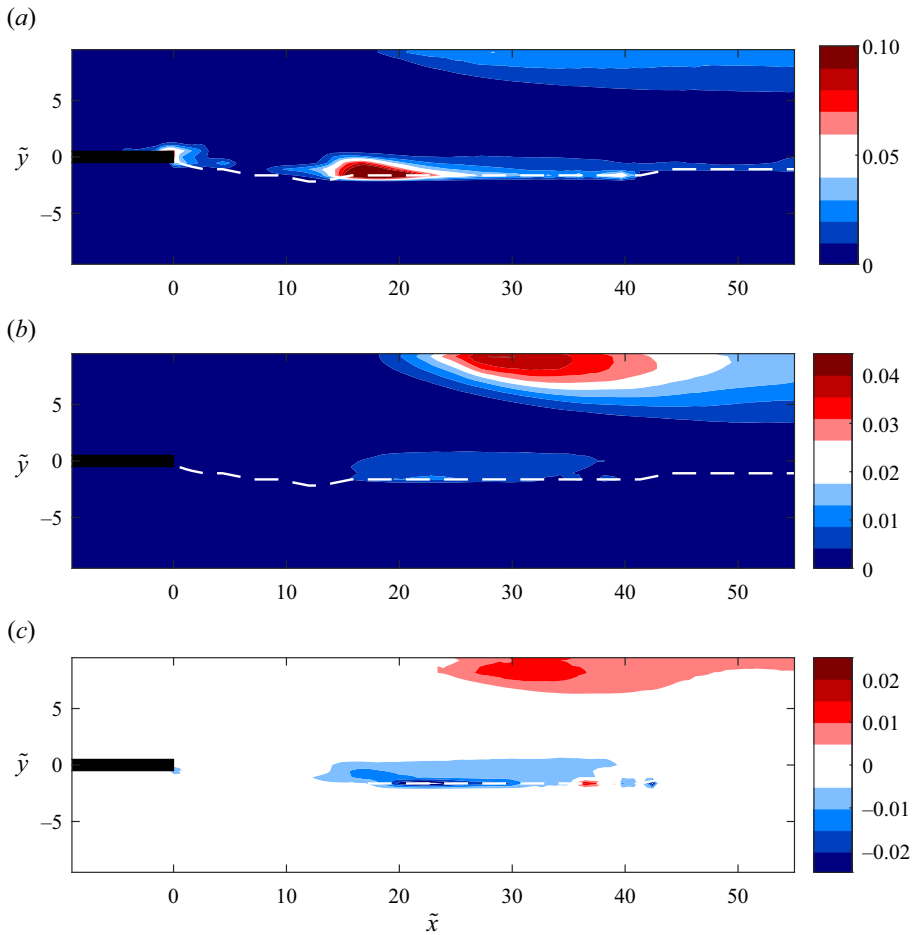
Figure 9. Contours of (a) $\overline{u'u'}/U_g^2$, (b) $\overline{v'v'}/U_g^2$ and (c) $\overline{u'v'}/U_g^2$. The splitter plate is highlighted in black, while the white dashed line denotes the time-averaged interface location. REF case of table 3.

(negative) measured value within the wake region (at the location $y^\star = y^\star_{min}$), and δ_d is an adjustable parameter introduced by Otto *et al.* (2013) to mimic experimental velocity profiles in the near-field region of the mixing layer.

Results of the comparison reveal a strict agreement between the measured and theoretical velocity profiles, both inside (i.e. negative value of velocity deficit) and outside the wake region. Values of the ratio δ_d/δ_g giving the best match with experimental data are respectively 0.75 (for $\tilde{x} < \tilde{x}_w$) and 0.78 ($\tilde{x} > \tilde{x}_w$). In agreement with Otto *et al.* (2013), we have $\delta_d/\delta_g < 1$ in both cases, due to the presence of a velocity deficit in the mean flow profile.

3.2. *Effect of liquid Reynolds number*

The effect of the liquid Reynolds number Re_l variation on the two-phase flow topology at fixed Re_g is investigated by modifying the injection velocity U_l. Results are shown in figure 12, where $\bar{u}(\tilde{y})$ distributions at different streamwise stations are reported for the REF and L3 cases, and in figure 13 in terms of time-averaged velocity magnitude contours and vectors distribution. The liquid Reynolds number varies between $Re_l = 302$ (L1 case) and
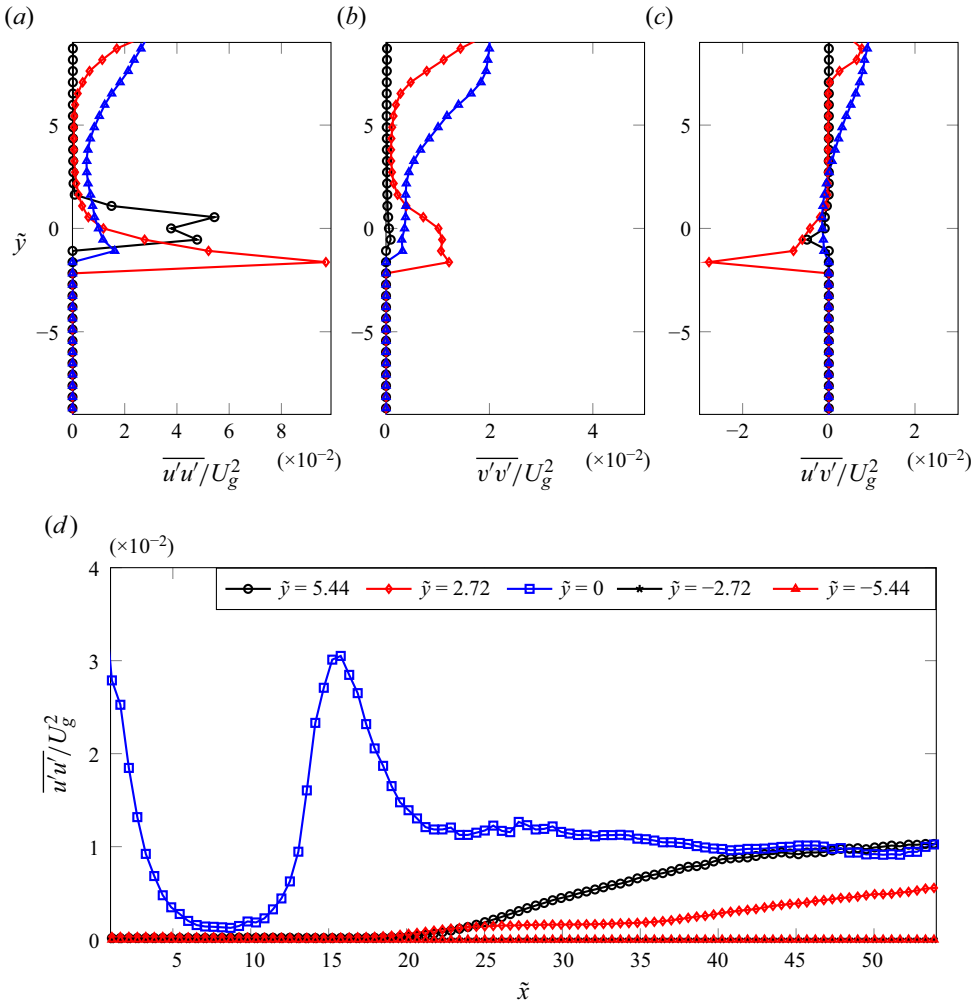
981 A13-15

Figure 10. Profiles of (*a*) $\overline{u'u'}/U_g^2$, (*b*) $\overline{v'v'}/U_g^2$ and (*c*) $\overline{u'v'}/U_g^2$ at different streamwise stations $\tilde{x}$: 0.55 (black circles), 21.76 (red diamonds), 53.31 (blue triangles). (*d*) Profiles of $\overline{u'u'}/U_g^2$ at different $\tilde{y}$ stations. REF case of table 3.

$Re_l = 807$ (L3 case), while the gas Reynolds number is $Re_g = 493$, as in the REF case discussed previously.

The velocity maps reported in figure 13 show that the recirculation region characterizing the flow immediately downstream of the injection section progressively reduces as Re_l increases, until it vanishes in the last (L3) case. The increase in inlet velocity of the liquid phase produces a shear effect at the interface, which accelerates locally the (transitional) gas flow and determines the progressive absorption of the wake. For the L3 case, the absence of the wake flow component determines an almost unperturbed air–water interface at the splitter plate edge. As a consequence, the two-phase mixing layer flow becomes spatially invariant along the streamwise direction up to $\tilde{y} = 5$ (see figure 12*b*), where differences among the streamwise-spaced velocity profiles are due to the presence of the air–air mixing layer, as observed previously in § 3.1.
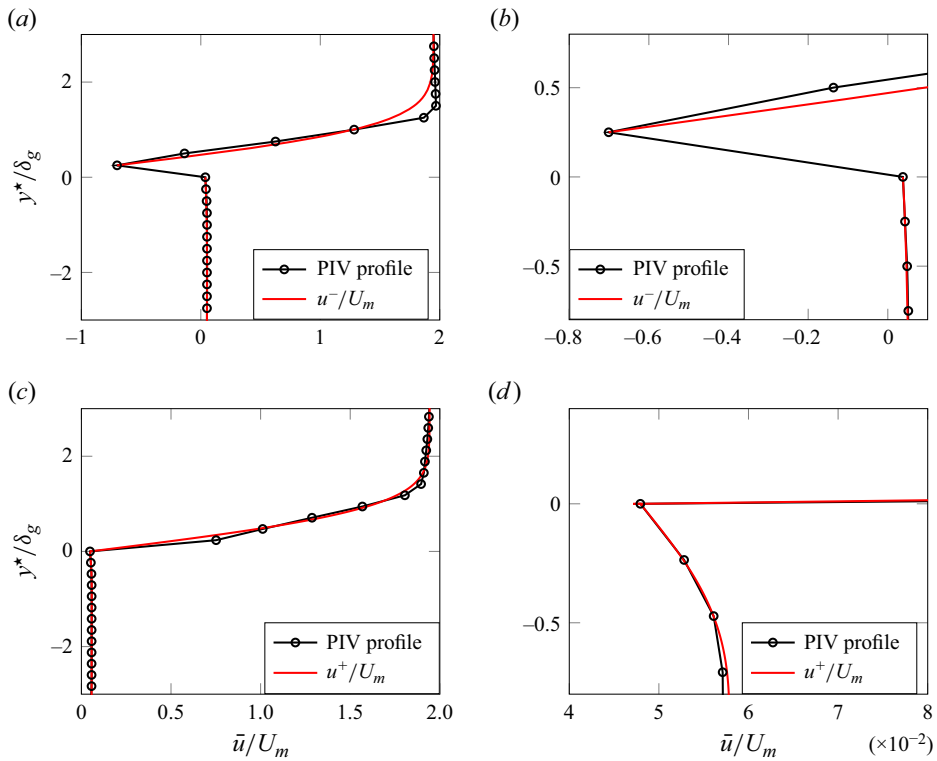
981 A13-16

Figure 11. Theoretical–experimental comparison of velocity profiles (a,b) inside ($\tilde{x} = 0.55$) and (c,d) outside ($\tilde{x} = 20.13$) the wake region of length $\tilde{x}_w = 17.5$. REF case of table 3.

It is important to note that when no wake is present due to a high Re_l value, the liquid velocity field is basically not influenced by the co-flowing gaseous phase, developing parallel to the streamwise direction and to the injected air stream (figure 13d). This aspect will be highlighted further in § 3.3, where the effect of the gas Reynolds number on the variation of the flow topology will be presented and compared with the present discussion. A complete parametric trend of the wake length as a function of Re_l for various Re_g values will also be shown in § 3.3.

3.3. *Effect of gas Reynolds number*

Results of the investigation performed by varying the gas Reynolds number are first shown in figures 14 and 15, respectively in terms of velocity magnitude contours with superposed vectors distributions, and $\bar{u}(\tilde{y})$ profiles at different streamwise locations; the liquid velocity is kept constant and equal to that of the REF case, so that $Re_l = 454$.

By looking at the two-dimensional flow fields in figures 14(a–c) and the velocity profiles in figure 15(a), it can be seen that the wake region shortens progressively by increasing Re_g from the G1 to the G3 case, with $\tilde{x}_w$ decreasing from 21.2 to 9.8. Accordingly, the peak of the Reynolds stress component $\overline{u'u'}$ is shifted towards lower $\tilde{x}$ values, and it achieves its maximum at $Re_g = 704$ (G2 case of table 3), as reported in figure 16. Due to the sudden change of the shear boundary condition downstream of the plate, the liquid velocity relaxes, and the water jet accelerates progressively and contracts along the streamwise direction x (Tillett 1968), as can be appreciated by looking at figures 14(a,b,c) in turn.
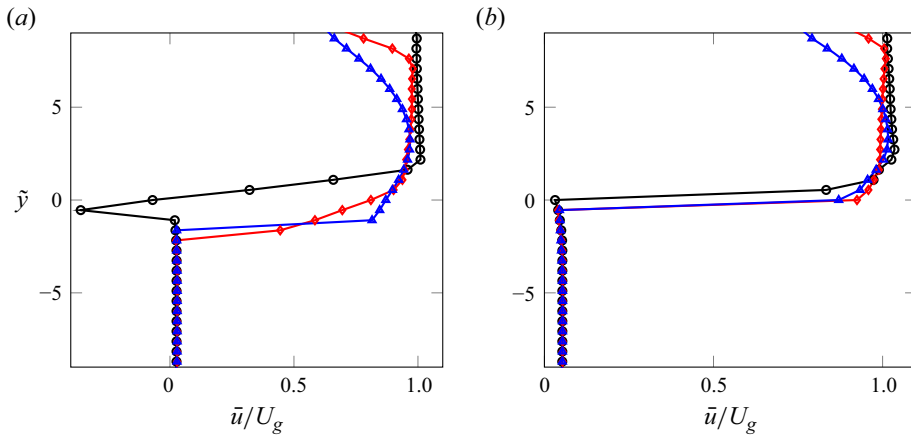
981 A13-17

Figure 12. Liquid Reynolds number Re_l effect on the time-averaged streamwise $\bar{u}(\tilde{y})/U_g$ velocity component at different $\tilde{x}$ stations: 0.55 (black circles), 21.76 (red diamonds), 53.31 (blue triangles). Cases (*a*) REF and (*b*) L3 of table 3.

Moreover, outside the wake region, the gas jet goes down progressively as Re_g increases (see also Agbaglah *et al.* 2017). The momentum flux difference in the air–air mixing layer also increases by increasing Re_g, leading to a reduction in $\bar{u}(\tilde{y})$ moving towards the top of the domain, as shown by the evolution of velocity profiles in figures 15(*b,c*).

For the highest value of gas Reynolds number considered (G4 case, see figure 14(*d*) and green curves in figure 15), the wake region vanishes, i.e. $\tilde{x}_w = 0$. As a consequence, no peak in the Reynolds stress component $\overline{u'u'}$ distribution is detected (blue curve in figure 16). It is important to note that when $\tilde{x}_w = 0$ due to a high Re_g value, the flow topology is significantly different from the case $\tilde{x}_w = 0$ at high Re_l discussed previously in § 3.2, as can be appreciated by comparing figures 14(*d*) and 13(*d*). As a matter of fact, the momentum exchanged by shear at the interface between the gas and liquid jets as Re_g increases accelerates the liquid, which then has to contract to conserve the mass flow rate (figure 14*d*). As a consequence, the flow is no longer spatially invariant along the streamwise direction, as instead it has been observed at high Re_l value (figure 13*d*).

An overall picture of the wake extension variation with Re_l and Re_g parameters is given in figure 17, where the trend $\tilde{x}_w(Re_l)$ is reported for different values of the gas Reynolds number Re_g, corresponding to the flow fields shown in figures 13 and 14. Note that additional cases characterized by a lower gas Reynolds number ($Re_g = 256$) have also been reported (black curve in figure 17). It can be seen that the progressive decreasing of the recirculation region with Re_l is enhanced by increasing the gas Reynolds number. At $Re_g = 768$, no wake is detected for any value greater than $Re_l = 302$ (orange curve in figure 17). The trend $\tilde{x}_w(Re_l)$ is qualitatively the same for all the other Re_g values: it is approximately constant up to $Re_l = 454$, then it decreases, reaching zero value for $Re_l = 807$.

3.4. *Effect of gas-to-liquid dynamic pressure ratio*

Finally, the trend of the wake length as a function of the gas-to-liquid dynamic pressure ratio M is summarized in figure 18, for different values of the gas Reynolds number. It can be seen that for a fixed Re_g, relatively low M values (high liquid velocities) promote a reduction of the wake, which vanishes eventually. This is analogous to the Re_l effect
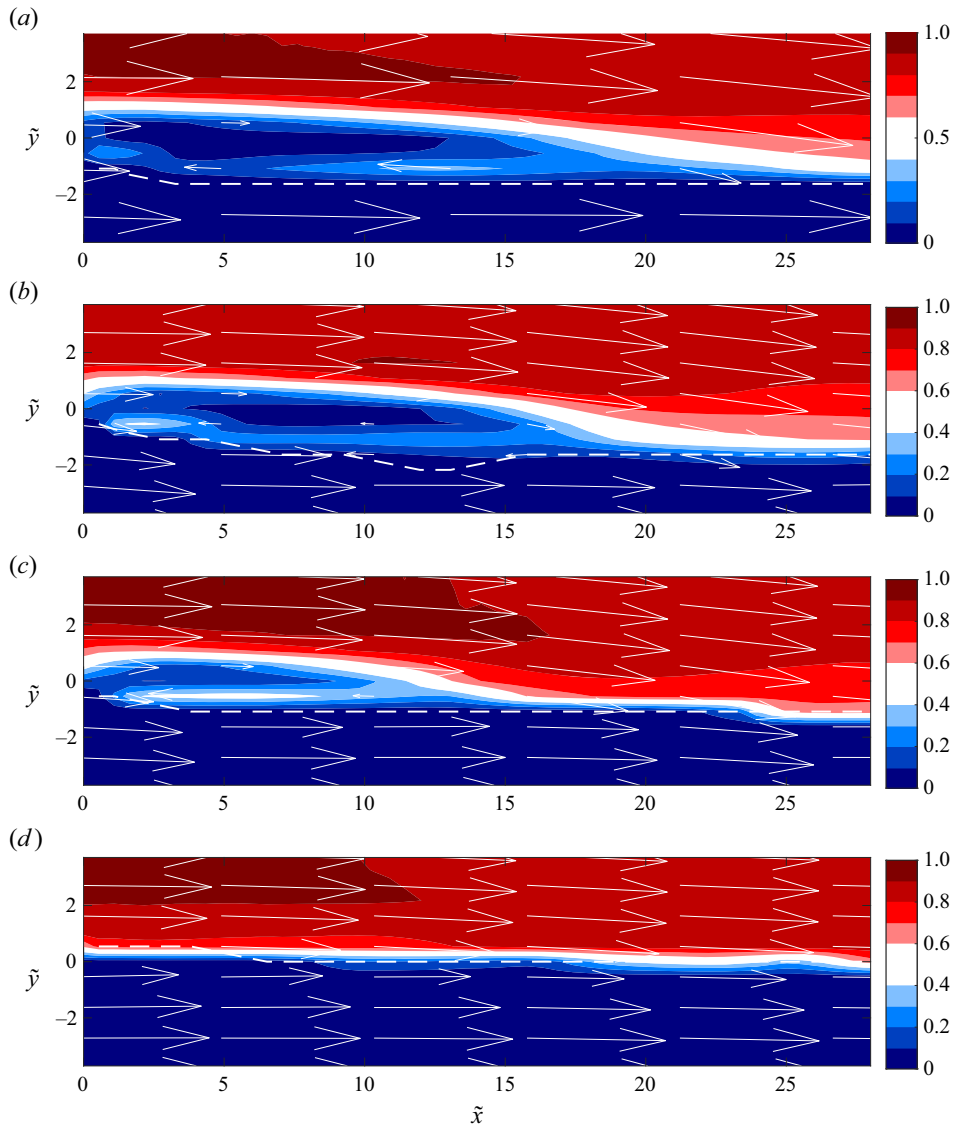
981 A13-18

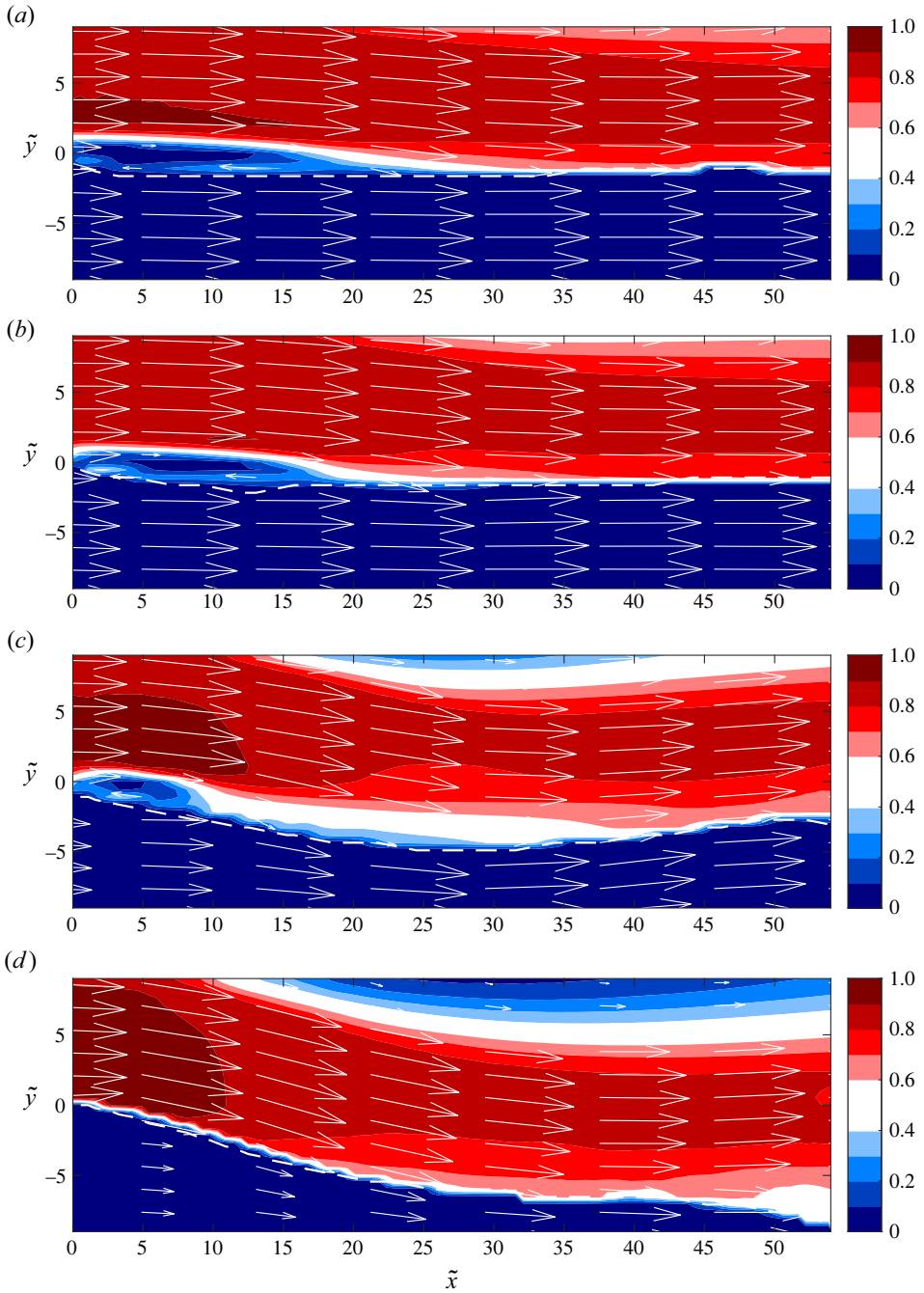Figure 13. Liquid Reynolds number Re_l effect on the time-averaged velocity magnitude $\bar{V}/U_g$. The mean interface location is represented as a white dashed line, and velocity vectors are also reported. Cases (*a*) L1, (*b*) REF, (*c*) L2 and (*d*) L3 of table 3.

outlined in figure 17 and by the velocity contours reported in figure 13. Moreover, the M value denoting the transition from a wake regime to a pure mixing layer regime increases with Re_g. Therefore, only at relatively high values of the gas Reynolds number does the flow behave as a pure mixing layer in a wide range of liquid injection velocities (i.e. wide range of M values).

As a first summary of the results concerning the mean (time-averaged) flow analysis, a comprehensive characterization of the flow fields in both the phases has been described, including velocity profiles in various streamwise stations, Reynolds stress tensor components, and wake size. The measured velocity profiles agree well with

981 A13-19

Figure 14. Gas Reynolds number Re_g effect on the time-averaged velocity magnitude $\bar{V}/U_g$. The mean interface location is represented as a white dashed line, and velocity vectors are also reported. Cases (*a*) G1, (*b*) REF, (*c*) G3 and (*d*) G4 of table 3.
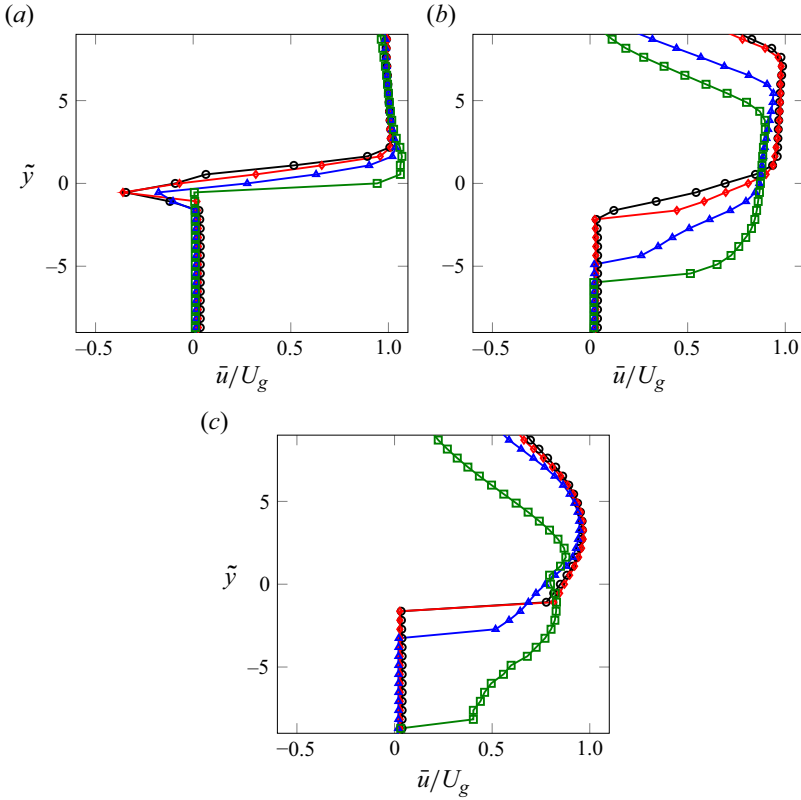
Figure 15. Gas Reynolds number Re_g effect on the time-averaged streamwise $\bar{u}(\tilde{y})/U_g$ velocity component at different $\tilde{x}$ stations: (*a*) 0.55, (*b*) 21.76, (*c*) 53.31. Cases G1 (black circles), REF (red diamonds), G3 (blue triangles) and G4 (green squares) of table 3.
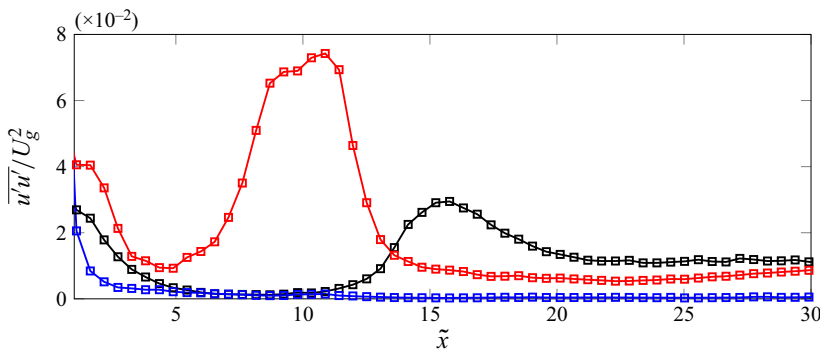
Figure 16. Profiles of $\overline{u'u'}/U_g^2$ at $\tilde{y} = 0$ for different values of the gas Reynolds number, for cases REF (black curve), G2 (red curve) and G4 (blue curve) of table 3.

analytical formulae proposed in past works for locally parallel flows in spatio-temporal stability analysis. The transition from a mixed wake mixing layer to a pure mixing layer regime as a function of the governing parameters has been highlighted. In §4, which reports the unsteady flow characteristics, the dominant flow oscillations will be interpreted
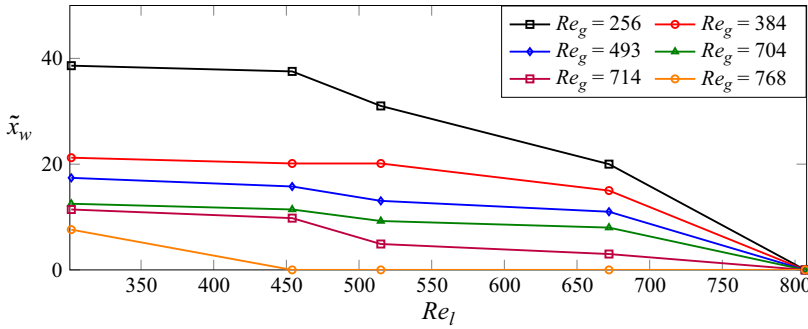
981 A13-21

Figure 17. Liquid Reynolds number Re_l effect on the wake region length $\tilde{x}_w$ at different Re_g values.
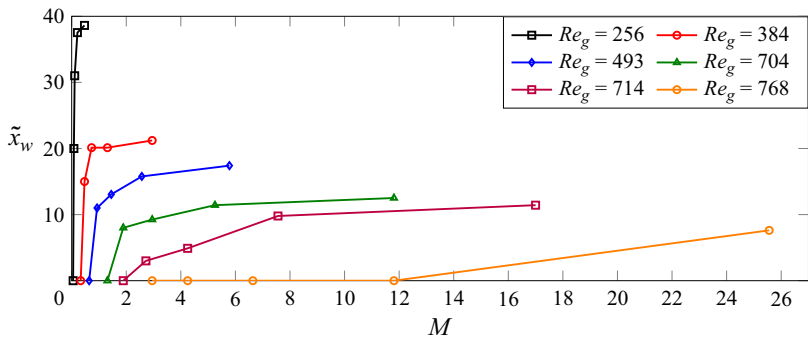

Figure 18. Dynamic pressure ratio M effect on the wake region length $\tilde{x}_w$ at different values of the gas Reynolds number Re_g.

in connection with the velocity profiles and the overall flow topology analysed here, giving insights into the global dynamics of the gas–liquid interface.

4. Unsteady flow characteristics

The unsteady development of the air–water mixing layer is first analysed by computing the power spectral density (PSD) of the PIV measurements of normal-to-flow velocity component fluctuations v', monitored at different $\tilde{x}$ and $\tilde{y}$ locations (white circles in figure 19). We start by focusing attention on the gas Reynolds number (Re_g) and the gas-to-liquid dynamic pressure ratio (M) effects on the frequency spectra evaluated at a monitoring station immediately downstream of the splitter plate in the air flow, namely $(\tilde{x}, \tilde{y}) = (0.55, 2.72)$.

Note that only frequency spectra in the high gas Reynolds number regime will be reported hereafter, for which we were able to identify a clear peak frequency. As a matter of fact, in the low Reynolds number regime ($Re_g \leq 493$), we found the frequency spectra to be very noisy and characterized by a high frequency content, the order of magnitude of the peak frequency being $O(f) = 10^2$ Hz. Moreover, we found the specific value of the peak frequency to be very sensitive to the selected spatial location. We believe that this occurrence is related to a noise amplifier behaviour exhibited by the flow in this regime, as already described by Otto *et al.* (2013) at relatively low M and Re_g values.

Results of the PSD of velocity signals are shown in figure 20, where two Re_g values are considered: $Re_g = 714$ (figures 20a,b) and $Re_g = 768$ (figure 20c,d). For each gas
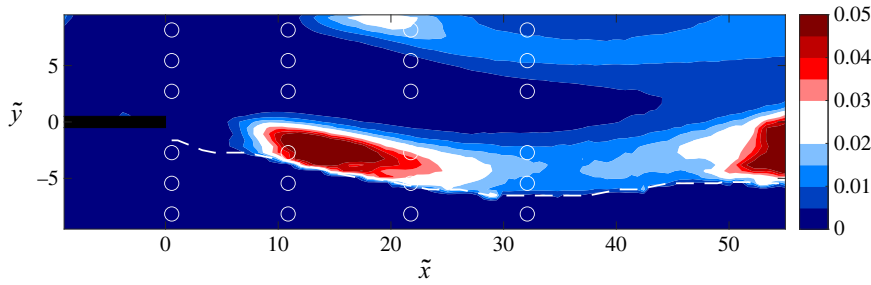
981 A13-22

Figure 19. Contour map of $\overline{v'v'}/U_g^2$ for the G5 case of table 3. The splitter plate is highlighted in black, while the white dashed line denotes the time-averaged interface location. The white circles denote the monitoring locations employed for the analysis of unsteady velocity fluctuations.
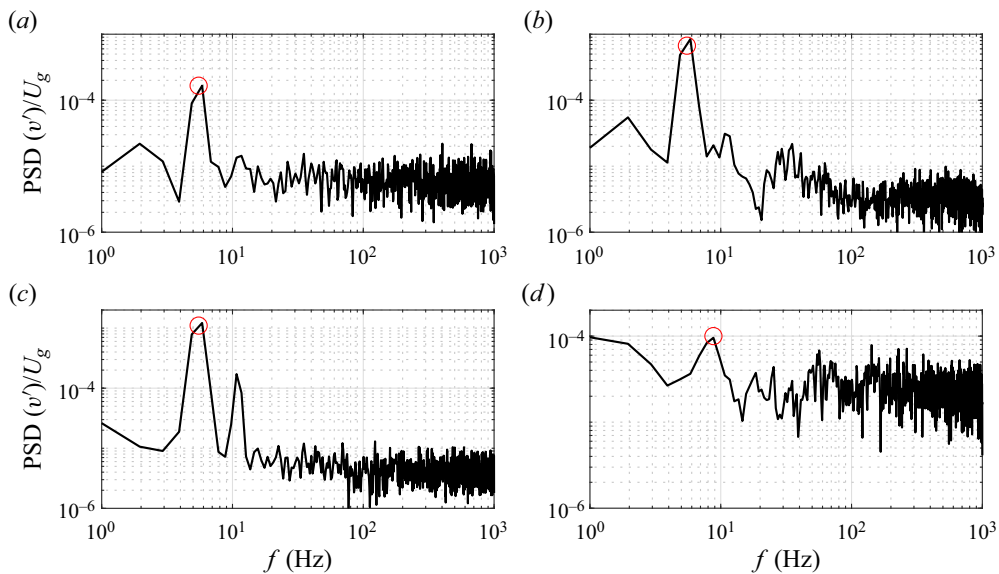

Figure 20. The PSD of normal-to-flow velocity component fluctuation $v'(t)/U_g$ at $(\tilde{x}, \tilde{y}) = (0.55, 2.72)$, i.e. in air flow immediately downstream of the splitter plate. The red circle denotes the peak frequency. Values are: (a) $Re_g = 714$, $M = 17.00$; (b) $Re_g = 714$, $M = 4.25$; (c) $Re_g = 768$, $M = 25.56$; (d) $Re_g = 768$, $M = 6.64$.

Reynolds number, we select two values of the gas-to-liquid dynamic pressure ratio parameter, respectively in the high ($M = 17.00$ and 25.56, figures 20a,c) and low ($M = 4.25$ and 6.64, figures 20b,d) M regimes. Note that the fluctuation amplitudes are made dimensionless by the inlet gas velocity value U_g corresponding to each case, while the dimensional frequency values are reported to facilitate comparison with a scaling law of literature.

For each Re_g considered, a clear peak frequency with order of magnitude $O(f) = 1$ Hz arises in the spectra shown in figure 20. In the low M regime (figures 20b,d), the peak frequency depends on the specific value of Re_g: it increases from $f = 5.86$ to $f = 8.79$ Hz for Re_g going from 714 (figure 20b) to 768 (figure 20d). The peak frequencies ratio between the latter and former case is 1.5, and it agrees well with the scaling $(U_{g(d)}/U_{g(b)})^{3/2} = 1.4$, where $U_{g(d)} = 15$ and $U_{g(b)} = 12$ m s^{-1}. This scaling was found in the experimental analyses by Raynal *et al.* (1997) and Marmottant & Villermaux (2004) for a multitude of
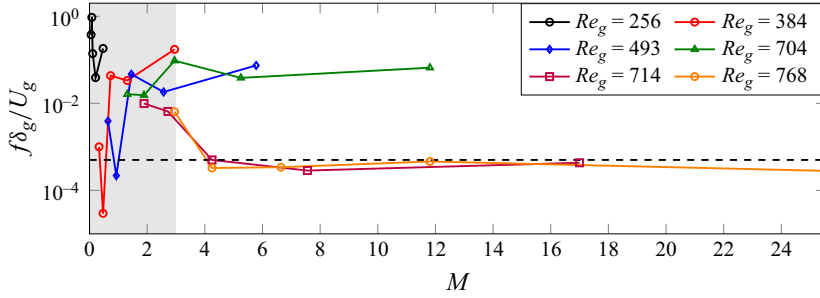
Figure 21. Dynamic pressure ratio M effect on the peak (dimensionless) frequency of the PSD of $v'(t)$ at $(\tilde{x}, \tilde{y}) = (0.55, 2.72)$ for different values of the gas Reynolds number Re_g. The plate-to-gas vorticity thickness ratio is $e/\delta_g > 1$ (see table 3 in § 3). The black dashed line denotes the peak Strouhal number found by Fuster *et al.* (2013) for $Re_g = 714$, $M = 16$ and $e/\delta_g < 1$.

gas injection velocity values. On the other hand, in the high M regime (figures 20a,c), the peak frequency does not depend on the specific Re_g value, being $f = 5.51$ Hz.

A significant data reduction, including measured peak frequencies for all the tested flow conditions, is also reported in figure 21, where the dimensionless peak frequencies $f\delta_g/U_g$ (Strouhal number) are shown as a function of M, for various values of Re_g. In spite of the uncertainty of the data in the low M regimes, this representation allows one to perform comparisons with previous theoretical predictions based on local spatio-temporal stability analyses and direct numerical simulations of the literature (Fuster *et al.* 2013; Otto *et al.* 2013; Bozonnet *et al.* 2022).

In particular, remember that for relatively low M and Re_g, Otto *et al.* (2013) found that the flow behaves like a noise amplifier (being characterized by convective instability). In these flow conditions, numerical simulations performed by Fuster *et al.* (2013) and lately by Bozonnet *et al.* (2022) have shown that frequency spectra of the gas–liquid interface oscillatory dynamics are very sensitive to the injected noise level (e.g. the turbulence fluctuations within the gas phase, characterized by high frequency values) and may depend on the selected streamwise station. On the contrary, at relatively high Re_g values, a transition from convective to absolute instability of the locally parallel flow was detected when M increases beyond a critical threshold M_c ($M_c = O(1)$ for $\rho_g/\rho_l = 0.001$ in Fuster *et al.* 2013). In this flow regime, the mixing layer acts as an oscillator, driving the unsteady dynamics to an intrinsic self-excited frequency not related to the noise perturbations spectrum. Moreover, Fuster *et al.* (2013) found that at relatively high Re_g, the dominant frequency is characterized by a monotonic decreasing trend approaching a constant value ($f\delta_g/U_g = O(10^{-4})$) as M increases.

The literature findings summarized above are recovered in the data distribution shown in figure 21. In particular, overall two distinct regimes can be detected as a function of M and Re_g parameters, which are well separated by the threshold value $M \approx 3$. For $M < 3$ (grey shaded area of figure 21), the high dispersion of frequency data recovers the typical behaviour of the noise amplifier regime discussed previously. On the other hand, the rather regular trends visible for high Re_g values (brown and orange curves) and $M > 3$ correspond to the intrinsic self-excited frequency regime, where a clear low-frequency peak ($f\delta_g/U_g = O(10^{-4})$) is observed. Note that the case $Re_g = 704$ (green curve) also belongs to the self-excited regime for $M > 3$, but it is characterized by a higher peak frequency, $f\delta_g/U_g = O(10^{-2})$.

981 A13-24

To compare further the data presented in this work with previous experimental findings from the literature, we note that by scaling the measured frequencies with respect to the reference value U_D/δ_g – where U_D is the celebrated Dimotakis velocity $U_D = (\sqrt{\rho_l}\, U_l + \sqrt{\rho_g}\, U_g)/(\sqrt{\rho_l} + \sqrt{\rho_g})$ (Dimotakis 1986) – a quantitative comparison with the results of Fuster *et al.* (2013) can be performed. In particular, figure 15 of Fuster *et al.* (2013) reports frequencies $f\delta_g/U_D$ as a function of the plate-to-gas vorticity thickness ratio e/δ_g, for a dynamic pressure ratio value $M = 16$. In the new frequency scale, the value $f\delta_g/U_D = O(10^{-2})$ is obtained for $M \approx 17$, which lies well within the range of measurements reported in figure 15 of Fuster *et al.* (2013). Moreover, it is interesting to note that the reduced frequency values $f\delta_g/U_g$ reported in figure 21 are consistent with the inviscid models proposed initially by Marmottant & Villermaux (2004), Raynal *et al.* (1997) and Raynal (1997), with the low values related to the low gas-to-liquid density ratio.

For the highest M value investigated here, corresponding to the G5 case of table 3, figures 22 and 23 report the frequency spectra at different stations along the streamwise direction, spanning the range $\tilde{x} \in [0.55, 32.10]$ (from (*a*) to (*d*) in each figure), in air and water flows, respectively. Each panel reports three curves, corresponding to three different $\tilde{y}$ locations in the air and water flows. The major finding is that the measured peak frequency does not vary moving along the streamwise and/or normal-to-flow direction. In other words, the velocity temporal fluctuations are synchronized at the same frequency over a large spatial extent of the flow field. As pointed out by Bozonnet *et al.* (2022), this may suggest the presence of a global mode. The POD analysis reported in §4.1 will give more insights on this aspect, and a summarizing discussion will accompany the conclusions.

Note that the unsteady dynamics of the G5 case is characterized by a low-order behaviour, i.e. the flow oscillates at the peak Strouhal number $f\delta_g/U_g = 2.8 \times 10^{-4}$ and the super-harmonic 5.6×10^{-4}, the energy content at other frequencies being much lower; a similar behaviour has been outlined recently for one-phase mixing layers formed between parallel streams of different velocities, by Dutta *et al.* (2022). The measured peak Strouhal number $f\delta_g/U_g = 2.8 \times 10^{-4}$ agrees well with other experimental findings reported in table 5 of Fuster *et al.* (2013). To facilitate the comparison, we report in figure 21 the peak Strouhal number measured by Fuster *et al.* (2013). It is worth noticing that this reference value (black dashed line in figure 21) was obtained for a plate-to-gas vorticity ratio $e/\delta_g < 1$, while the frequency data presented here all correspond to $e/\delta_g > 1$ (see table 3 in §3). Therefore, a significant conclusion of this work is that for the largest values of Re_g and M, the peak frequencies are not influenced by the splitter plate thickness.

4.1. *Proper orthogonal decomposition and interfacial dynamics*

To elucidate in more depth the spatio-temporal flow topology in presence of synchronized velocity oscillations, the analysis of the G5 case is broadened by performing a modal decomposition analysis, namely the POD of momentum fluctuations $\rho v'$:

$$\rho\, v'(\tilde{x}, \tilde{y}, t) = \rho\, v(\tilde{x}, \tilde{y}, t) - \overline{\rho v}\,(\tilde{x}, \tilde{y}) = \sum_{j=1}^{\infty} a_j(t)\, \varphi_j(\tilde{x}, \tilde{y}), \qquad (4.1)$$

where the density ρ is equal to ρ_l (ρ_g) in the liquid (gas) phase (see table 2 in §3). The gappy POD iterative algorithm (Everson & Sirovich 1995; Venturi & Karniadakis 2004; Gunes, Sirisup & Karniadakis 2006) is applied to de-noise the data and extract the leading
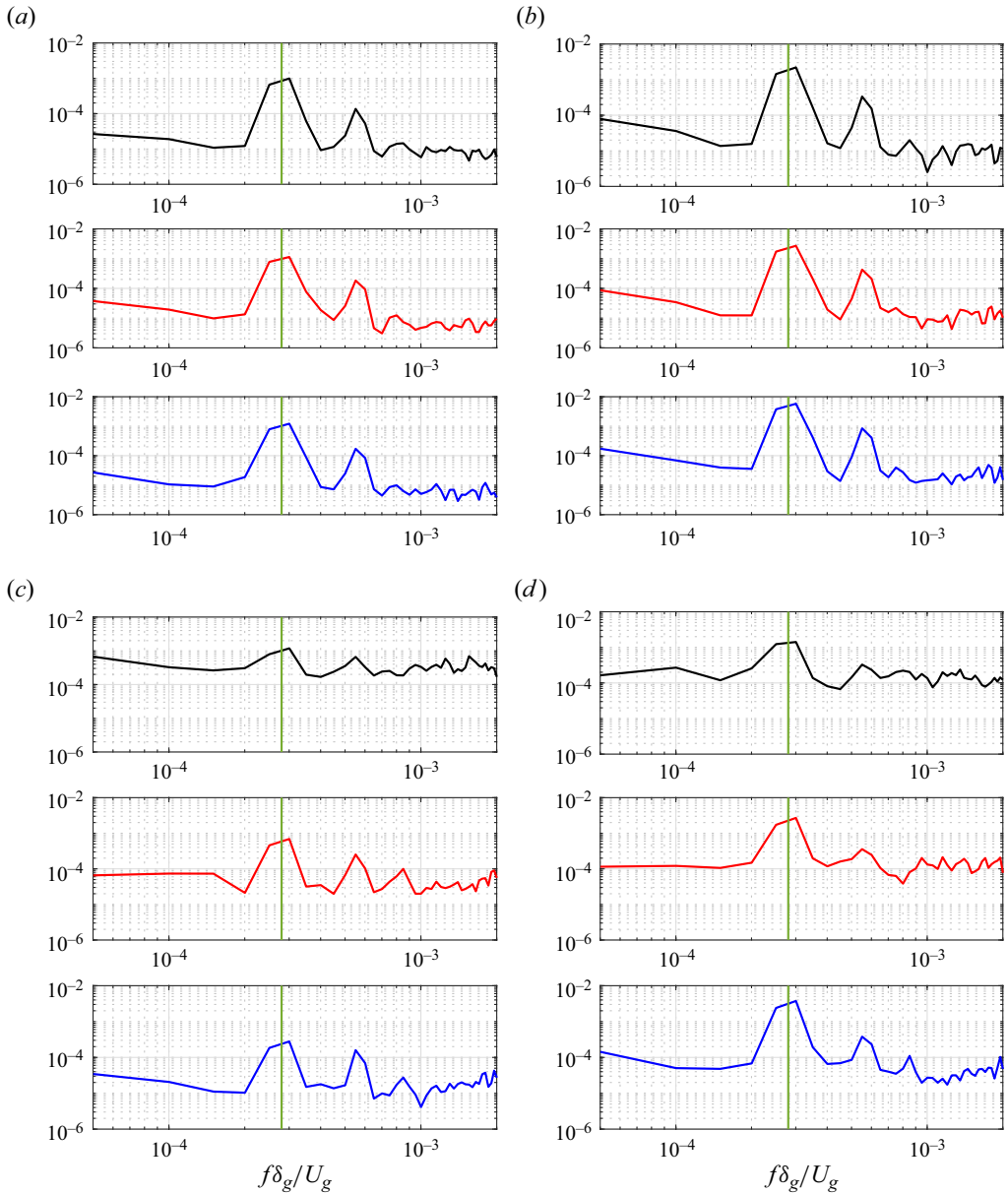
Figure 22. The PSD of $v'(t)/U_g$ at different $(\tilde{x}, \tilde{y})$ locations in air flow, for $\tilde{y}$ values 8.16 (black curve), 5.44 (red curve), 2.72 (blue curve). The vertical green line denotes the peak dimensionless frequency $f\delta_g/U_g = 2.8 \times 10^{-4}$. Case G5 of table 3. Values are: (*a*) $\tilde{x} = 0.55$, (*b*) $\tilde{x} = 10.88$, (*c*) $\tilde{x} = 21.76$, (*d*) $\tilde{x} = 32.10$.

modes, with a spatial weight matrix (defining the state vector norm) accounting for the different densities of gas and liquid phases. The POD analysis is carried out in the spatial region $x \in [-5, 30] \times y \in [-10, 5]$, i.e. around the gas–liquid interface.

Results are reported in figure 24 in terms of energy distribution (figure 24*a*) and the topology of the leading five modes (figures 24*b–f*), and in figure 25, which shows the PSD of the corresponding temporal coefficients a_i. The first mode has a 23 % energy content and represents a normal-to-flow flapping motion of the interface (figure 24*b*). The PSD
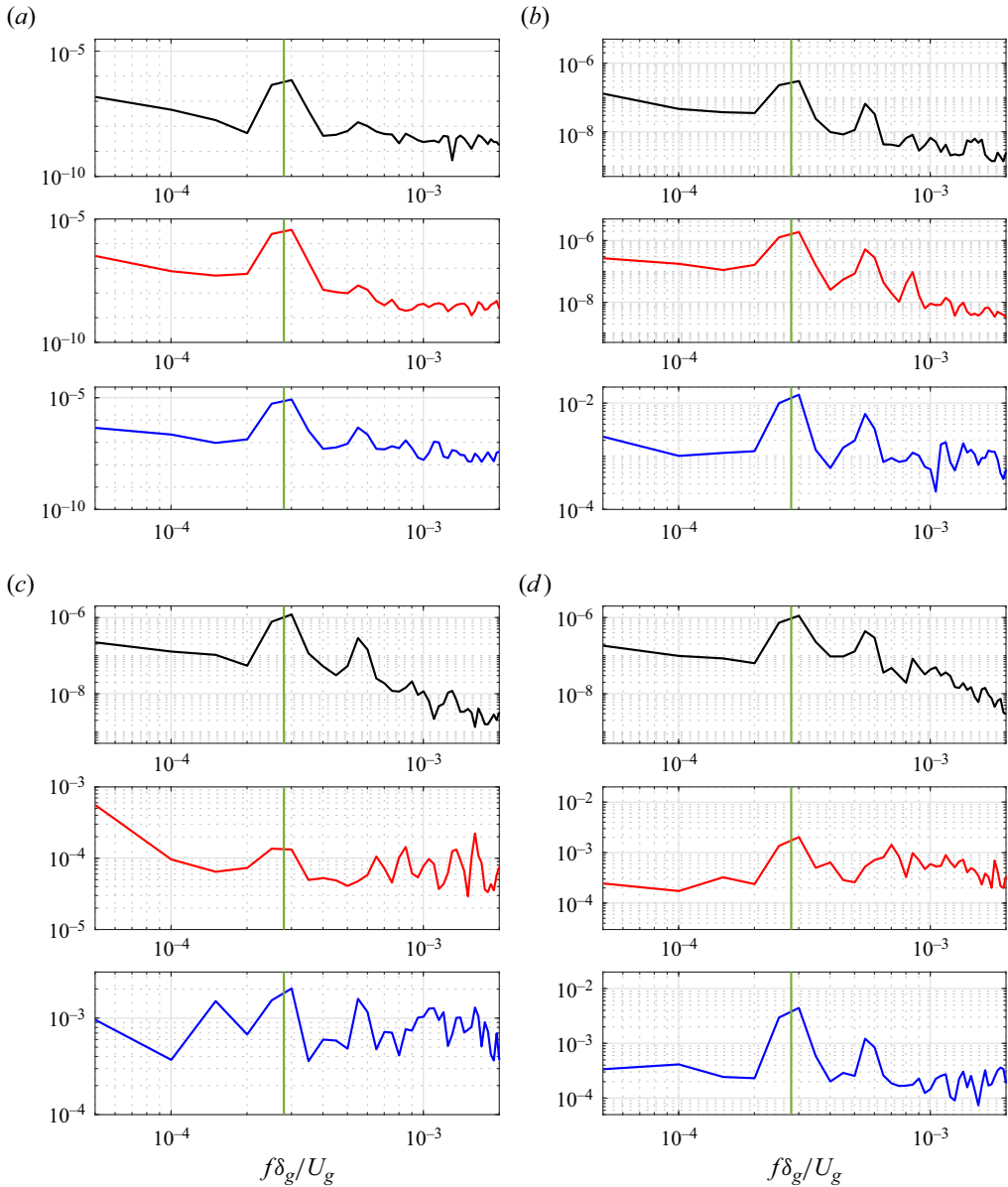
981 A13-26

Figure 23. The PSD of $v'(t)/U_g$ at different $(\tilde{x}, \tilde{y})$ locations in water flow, for $\tilde{y}$ values -8.16 (black curve), -5.44 (red curve), -2.72 (blue curve). The vertical green line denotes the peak dimensionless frequency $f\delta_g/U_g = 2.8 \times 10^{-4}$. Case G5 of table 3. Values are: (*a*) $\tilde{x} = 0.55$, (*b*) $\tilde{x} = 10.88$, (*c*) $\tilde{x} = 21.76$, (*d*) $\tilde{x} = 32.10$.

of the associated temporal coefficient a_1 reveals a peak frequency $f\delta_g/U_g = 2.8 \times 10^{-4}$ (figure 25), which is the same value found in the local spectral analyses shown previously in figure 22. This finding reveals that the synchronized velocity oscillations measured within the gas and liquid phases are determined by a flapping mode of the gas–liquid interface, which therefore rules the whole flow field dynamics. The other leading modes are associated with different flow coherent structures. In particular, the pair of 2nd and 3rd modes (containing 8.5 % and 7.2 % energy, respectively) and 4th and 5th modes (containing 5.4 % and 4.0 % energy, respectively) represent interfacial travelling waves
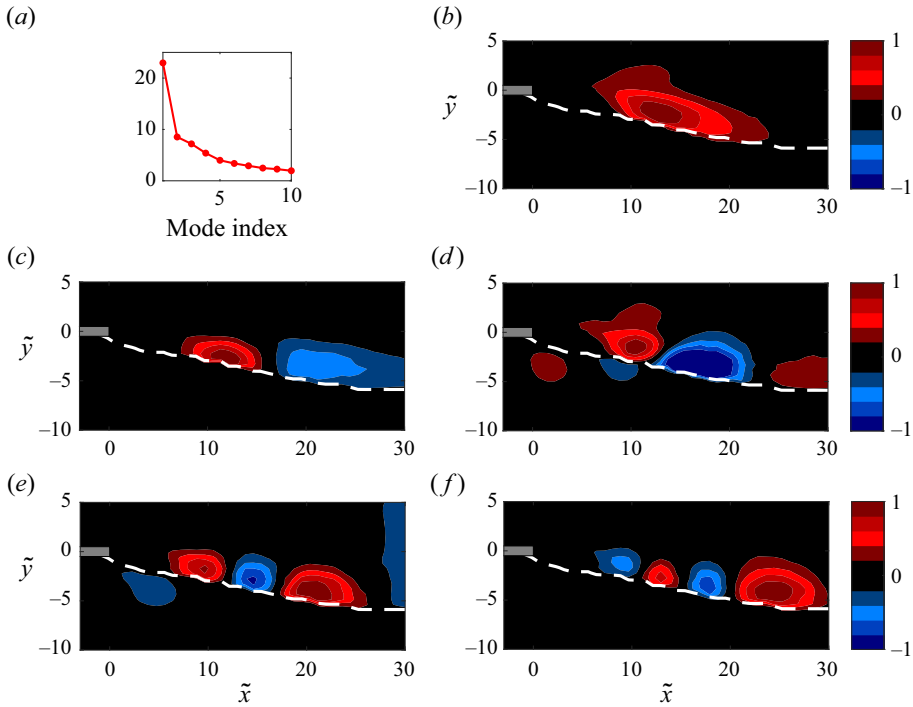
981 A13-27

Figure 24. POD analysis of the G5 case of table 3. (*a*) POD modes energy distribution (%). (*b*–*f*) Leading modes (1st to 5th, respectively, each scaled with respect to its maximum). In each plot, the splitter plate is highlighted in grey, and the mean interface location is denoted by the white dashed line.

advected along the streamwise direction, each couple being characterized by the typical shift of modes along the $\tilde{x}$ axis (figure 24*c*–*f*).

To obtain an estimate of the order of magnitude of the flapping mode frequency, literature data measured in analogous flow configurations of separated flows past a backward facing ramp (Chiatto, luca & Grasso 2021), or more generally in the presence of a separation bubble (Kiya & Sasaki 1983), have been considered, although these data were taken for bubbles forming in single phase flows. Following Chiatto *et al.* (2021), who expressed the Strouhal number in terms of the flow reattachment length, in the present context it has been assumed that the length of the flapping interface coincides with practically the entire length of the test section, i.e. $\lambda = 250e$. As a consequence, it has been found that $St = f\lambda/U_g = O(10^{-1})$, which agrees well with values reported in the studies cited above.

It is interesting to note that multiplying the second POD mode wavelength $\lambda = 25e$ (figure 24*c*) by the secondary peak frequency of the PSD (*a*₂), $f\delta_g/U_g = 5.6 \times 10^{-4}$ (figure 25), one can infer the dimensional velocity of the travelling disturbance wave, i.e. $U = \lambda f = 0.55$ m s^{-1}. This value is in close agreement with the interfacial wave propagation speed given by Dimotakis (1986), $U_D = 0.59$ m s^{-1} (relative spread 6.78 % for $U_l = 0.1$ m s^{-1} and $U_g = 15$ m s^{-1}, corresponding to the G5 case analysed here), which was obtained assuming the gas and liquid dynamic pressures to be in balance in a reference frame moving with the wave speed. Moreover, the mode wavelength is of the same order as the gas injector size, namely $\lambda/H_g = 2.5$.
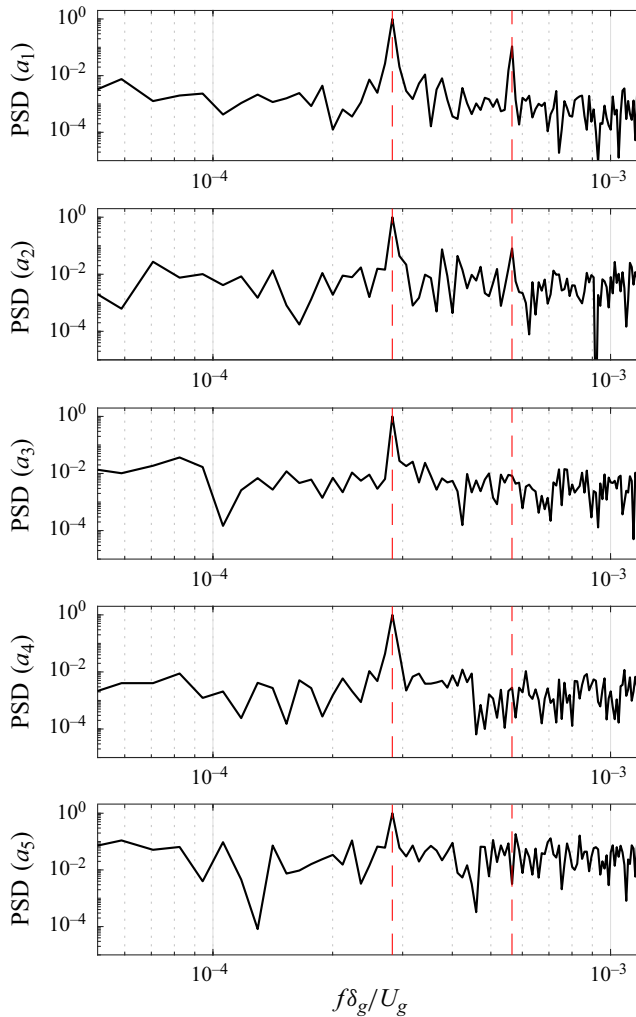
981 A13-28

Figure 25. The PSD of the temporal coefficients a_i associated with the leading POD modes shown in figure 24. The vertical red dashed lines denote the peak frequency $f\delta_g/U_g = 2.8 \times 10^{-4}$ and its first super-harmonic $f\delta_g/U_g = 5.6 \times 10^{-4}$.

The synchronized velocity oscillations associated with the flapping mode in the G5 case are retrieved also in the G4 case, whose time-averaged flow shows no wake (as shown previously in figure 14d). This can be appreciated by looking at figures 26(a,b), respectively showing the flapping modes of the G5 and G4 cases (the modes energy distributions of the two cases are reported in figure 27, red and blue curves, respectively). Observe also that for the G4 case, the interface flapping is not associated with the presence of any wake. In general, the flapping mode occurs only at high Re_g and M values; as a matter of fact, none of the cases analysed here below the threshold value $M \approx 3$ exhibits this mode. Figure 27 shows also that both cases G5 and G4 feature a low-order behaviour. In summary, at high Re_g values, independently of the presence of the wake, the dominant global flow structure is represented by the flapping mode of the interface, with oscillations synchronized in all the stations.
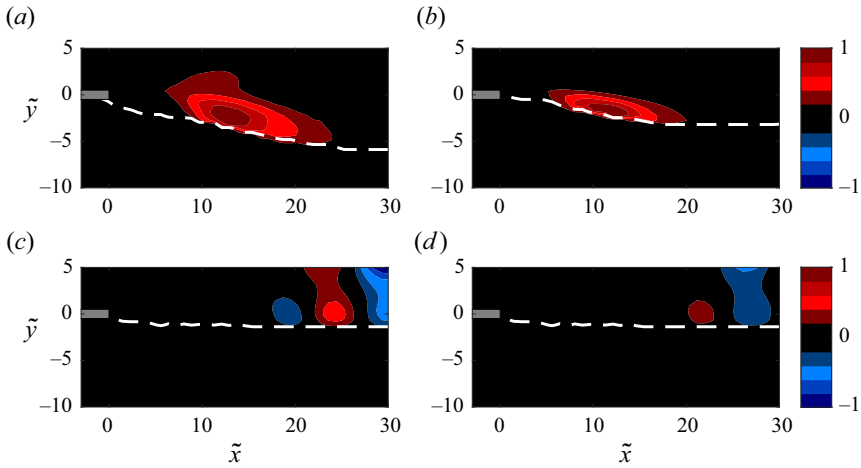
Figure 26. The first POD modes of the cases (*a*) G5, (*b*) G4 and (*c*) REF of table 3. (*d*) The second POD mode of the REF case. In each plot, the splitter plate is highlighted in grey, the mean interface location is denoted by the white dashed line, and each mode is scaled with respect to its maximum.
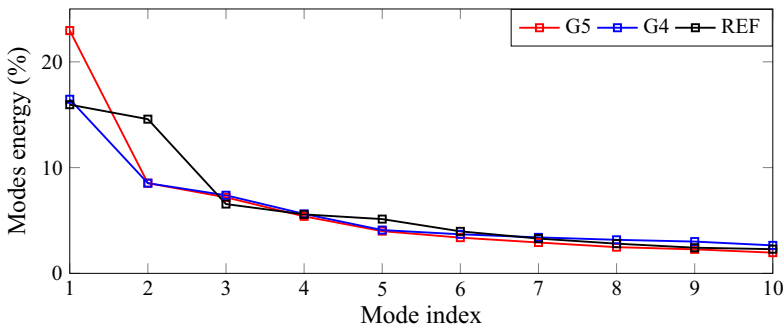

Figure 27. The POD modes energy distribution of the G5 (red curve), G4 (blue curve) and REF (black curve) cases of table 3.

For lower values of Re_g, the dominant structures are represented by a sort of fingers shedding, oscillating at higher frequency. This is shown for the REF case in figures 26(*c,d*) (the corresponding modes energy distribution is reported in figure 27, black curve). The pair of 1st and 2nd modes of the REF case represents a shedding mode of the gas phase, which is characterized by a dimensionless frequency $f\delta_g/U_g = O(10^{-2})$, significantly higher than the flapping dynamics frequency $f\delta_g/U_g = 2.8 \times O(10^{-4})$ identified previously. As a more general result, the low Re_g regimes feature the presence of the wake, and the shedding of finger structures represents the dominant modes oscillating at higher frequency. For the REF case reported here, figure 27 indicates that the low-order behaviour is no longer valid, the energy being distributed almost evenly among the modes.

5. Conclusions

The mean (time-averaged) flow topology and the unsteady flow characteristics of a planar mixing layer originating from the interaction of parallel air and water streams, which are initially separated by a plate, have been investigated experimentally. By means of

a single-laser single-camera experimental set-up, time-resolved PIV measurements of the flow have been performed simultaneously in the gaseous and liquid streams. The paper aims to clarify further the mechanisms leading to the flow breakup in gas-assisted atomization. Indeed, it is known that the statistics of multiphase turbulence in the mixing layer are influenced strongly by the interfacial dynamics. The complete experimental characterization of the velocity field represents a database that could be used in data-driven reduced-order models to investigate the global behaviour of the flow system.

A selected reference configuration ($Re_l = 454$, $Re_g = 493$) has been analysed first, showing that the mean two-phase flow is affected by the presence of a wake region downstream of the splitter plate. A strict agreement between the experimental data and theoretical velocity profiles provided in literature (Fuster *et al.* 2013; Otto *et al.* 2013) has been observed, both in the pure mixing layer region and inside the wake, where a negative value of the velocity deficit (difference between the minimum and free-stream liquid velocity) has been found. Then the mean flow topology has been investigated by varying the liquid (Re_l) and gas (Re_g) Reynolds numbers, and as a consequence also the gas-to-liquid dynamic pressure ratio (M). For a given Re_g, the wake region reduces progressively as Re_l increases (M decreases), and eventually vanishes. In the last condition, the air–water mixing layer becomes parallel, namely spatially invariant along the streamwise direction. Analogously, the wake shortens progressively as Re_g increases for a fixed Re_l, and for the highest value of the gas Reynolds number considered here ($Re_g = 768$), it vanishes in a wide range of M values ($M < 12$). Therefore, it has been found that only at relatively high values of the gas Reynolds number does the flow behave as a pure mixing layer in a wide range of liquid injection velocities.

The unsteady flow characteristics have been investigated next by analysing the frequency spectra of normal-to-flow velocity fluctuations, evaluated at different locations within both the air and water phases. For high Re_g configurations, it has been found that a low-frequency peak $f\delta_g/U_g = 2.8 \times 10^{-4}$ arises as M increases progressively beyond the threshold value $M \approx 3$. The peak frequency does not depend on the spatial location, i.e. the velocity fluctuations in air and water flows are synchronized over a large spatial region, which may suggest the presence of a global mode of instability. Moreover, the peak frequency agrees well with the experimental findings reported in Fuster *et al.* (2013), which were obtained for a plate-to-gas vorticity ratio $e/\delta_g < 1$. Since the frequency data presented in this work all correspond to $e/\delta_g > 1$, a significant conclusion is that for the largest values of Re_g and M, the peak frequencies are not influenced by the splitter plate thickness. On the contrary, for low Re_g and M regimes, the spectra are characterized by a high frequency content, and the peaks show a high dispersion, depending on the selected spatial location and accuracy of the measurements.

For flow conditions corresponding to the highest Re_g and M values investigated, the proper orthogonal decomposition (POD) of velocity fluctuations has been performed finally, to confirm the frequency response findings and to give insights into the major coherent structures of the flow. The POD analysis has revealed that the synchronized velocity oscillations, measured in both gas and liquid phases, are associated with a globally dominant flapping motion of the gas–liquid interface as a whole, independently of the presence of the wake bubble. Higher-order modes correspond to interfacial wave structures travelling with the so-called Dimotakis velocity. For relatively high Re_g values, the flow system reveals a low-order behaviour, because the energy content of the dominant mode (flapping structure) is much larger than that of the other modes. For lower gas Reynolds numbers, the leading modes correspond to fingers shedding at the interface, in general

in the presence of wake. In these last regimes, the low-order behaviour is lost, the POD analysis showing that the energy is almost evenly distributed among the modes.

The authors believe that this paper constitutes a step ahead in the comprehension of the dynamics of two-phase mixing layer flows produced by a separator plate because, by making use of accurate experimental measurements and modal decomposition analysis, it shed lights on some phenomena that remained unclear from previous studies. For instance, Fuster *et al.* (2013) claimed: 'The fact that both numerical and experimental spectra become more noisy when e/δ_g increases is analogous to the transition from absolute to convective instability observed when the dynamic pressure ratio is decreased. This is counter-intuitive because thick splitter plates help to create large velocity deficits, and therefore one would instead expect them to enhance absolute instability. Simulation results have revealed that the contact line travels up and down the leading edge of the separator plate, which may explain the significant amount of noise observed in the spectra. However it is difficult to conclude whether the dynamics of the contact line are responsible for the frequency shift or not. We therefore believe that the frequency shift is a consequence of the flow created behind the separator plate and not of the contact line dynamics.' We hope that the present work has given a contribution in resolving this issue, and actually it seems that the dominant frequency of the contact line dynamics is due to the presence of the flapping mode.

Author ORCIDs.

- Alessandro Della Pia https://orcid.org/0000-0003-2989-4397;
- Theodoros Michelis https://orcid.org/0000-0003-4836-6346;
- Matteo Chiatto https://orcid.org/0000-0002-5080-7756;
- Marios Kotsonis https://orcid.org/0000-0003-0263-3648;
- Luigi de Luca https://orcid.org/0000-0002-1638-0429.

REFERENCES

AGBAGLAH, G., CHIODI, R. & DESJARDINS, O. 2017 Numerical simulation of the initial destabilization of an air-blasted liquid layer. *J. Fluid Mech.* **812**, 1024–1038.

ANDRÈ, M.A. & BARDET, P.M. 2015 Interfacial shear stress measurements using high spatial resolution multiphase PIV. *Exp. Fluids* **56** (132), 1–18.

AYATI, A.A., KOLAAS, J., JENSEN, A. & JOHNSON, G.W. 2014 A PIV investigation of stratified gas–liquid flow in a horizontal pipe. *Intl J. Multiphase Flow* **61**, 129–143.

BEN RAYANA, F., CARTELLIER, A. & HOPFINGER, E. 2006 Assisted atomization of a liquid layer: investigation of the parameters affecting the mean drop size prediction. In *Proceedings ICLASS 2006*.

BOECK, T. & ZALESKI, S. 2005 Viscous versus inviscid instability of two-phase mixing layers with continuous velocity profile. *Phys. Fluids* **17**, 032106.

BOZONNET, C., MATAS, J.P., BALARAC, G. & DESJARDINS, O. 2022 Stability of an air–water mixing layer: focus on the confinement effect. *J. Fluid Mech.* **933** (A14), 1–27.

BUCKLEY, M.P. & VERON, F. 2017 Airflow measurements at a wavy air–water interface using PIV and LIF. *Exp. Fluids* **58** (161), 1–20.

CHIATTO, M., DE LUCA, L. & GRASSO, F. 2021 Modal analysis of actively controlled flow past a backward facing ramp. *Phys. Rev. Fluids* **6**, 064608.

COLANERA, A., DELLA PIA, A. & CHIATTO, M. 2022 Data-driven global stability of vertical planar liquid jets by dynamic mode decomposition on random perturbations. *Phys. Fluids* **34**, 122101.

DESCAMPS, M.N., MATAS, J.P. & CARTELLIER, A. 2008 Gas–liquid atomisation: gas phase characteristics by PIV measurements and spatial evolution of the spray. In *2nd Colloque INCA, Initiative en Combustion Avancèe*.

DIMOTAKIS, P.E. 1986 Two-dimensional shear layer entrainment. *AIAA J.* **24** (11), 1791–1796.

DUTTA, D., KANSHANA, I., GOPALAKRISHNAN, S.S. & MANDAL, A.C. 2022 Experimental studies on the frequency selection in flat plate wakes: mean-flow stability analyses and low-dimensional modeling. *Phys. Rev. Fluids* **7**, 044102.

EGGERS, J. & VILLERMAUX, E. 2008 Physics of liquid jets. *Rep. Prog. Phys.* **71**, 036601.

EVERSON, R.M. & SIROVICH, L. 1995 Karhunen–Loève procedure for gappy data. *J. Opt. Soc. Am.* A **12**, 1657–1664.

FUSTER, D., MATAS, J.P., MARTY, S., POPINET, S., HOEPFFNER, J., CARTELLIER, A. & ZALESKI, S. 2013 Instability regimes in the primary breakup region of planar coflowing sheets. *J. Fluid Mech.* **736**, 150–176.

GROTH, J. & JOHANSSON, A.V. 1988 Turbulence reduction by screens. *J. Fluid Mech.* **197**, 139–155.

GUNES, H., SIRISUP, S. & KARNIADAKIS, G. 2006 Gappy data: to Krig or not to Krig? *J. Comput. Phys.* **212** (1), 358–382.

HELMHOLTZ, H. 1868 On discontinuous movements of fluids. *Lond. Edinb. Dublin Philos. Mag. J. Sci.* **36** (244), 337–346.

JIANG, D. & LING, Y. 2020 Destabilization of a planar liquid stream by a co-flowing turbulent gas stream. *Intl J. Multiphase Flows* **122**, 103–121.

JIANG, D. & LING, Y. 2021 Impact of inlet gas turbulence on the formation, development and breakup of interfacial waves in a two-phase mixing layer. *J. Fluid Mech.* **921**, A15.

KIM, J., MOIN, P. & MOSER, R. 1987 Turbulence statistics in fully developed channel flow at low Reynolds number. *J. Fluid Mech.* **177**, 133–166.

KIYA, M. & SASAKI, K. 1983 Structure of a turbulent separation bubble. *J. Fluid Mech.* **137**, 83–113.

KOSIWCZUK, W., CESSOU, A., TRINITÈ, M. & LECORDIER, B. 2005 Simultaneous velocity field measurements in two-phase flows for turbulent mixing sprays by means of two-phase PIV. *Exp. Fluids* **39**, 895–908.

LEFEBVRE, A.H. 1989 *Atomization and Sprays*. Emisphere Publishing.

LI, H., FERNEX, D., SEMAAN, R., TAN, J., MORZYŃSKI, M. & NOACK, B.R. 2021 Cluster-based network model. *J. Fluid Mech.* **906**, A21.

LING, Y., FUSTER, D., TRYGGVASON, G. & ZALESKI, S. 2019 A two-phase mixing layer between parallel gas and liquid streams: multiphase turbulence statistics and influence of interfacial instability. *J. Fluid Mech.* **859**, 268–307.

LING, Y., FUSTER, D., ZALESKI, S. & TRYGGVASON, G. 2017 Spray formation in a quasiplanar gas–liquid mixing layer at moderate density ratios: a numerical closeup. *Phys. Rev. Fluids* **2** (1), 014005.

MARMOTTANT, P. & VILLERMAUX, E. 2004 On spray formation. *J. Fluid Mech.* **498**, 73–111.

MARSHALL, R.D. 1985 Performance requirements and preliminary design of a boundary layer wind tunnel facility. US Department of Commerce NBSIR 85-3168.

MATAS, J.P. 2015 Inviscid versus viscous instability mechanism of an air–water mixing layer. *J. Fluid Mech.* **768**, 375–387.

MATAS, J.P., DELON, A. & CARTELLIER, A. 2018 Shear instability of an axisymmetric air–water coaxial jet. *J. Fluid Mech.* **843**, 575–600.

MATAS, J.P., MARTY, S. & CARTELLIER, A. 2011 Experimental and analytical study of the shear instability of a gas–liquid mixing layer. *Phys. Fluids* **23**, 094112.

MATAS, J.-P., MARTY, S., DEM, M.S. & CARTELLIER, A. 2015 Influence of gas turbulence on the instability of an air–water mixing layer. *Phys. Rev. Lett.* **115**, 074501.

MEHTA, R.D. 1991 Effect of velocity ratio on plane mixing layer influence of the splitter plate wake. *Exp. Fluids* **10**, 194–204.

MEHTA, R.D. & BRADSHAW, P. 1979 Design rules for small low speed wind tunnels. *Aeronaut. J. R. Aeronaut. Soc.* **827**, 443–452.

OTTO, T., ROSSI, M. & BOECK, T. 2013 Viscous instability of a sheared liquid–gas interface: dependence on fluid properties and basic velocity profile. *Phys. Fluids* **25**, 032103.

RAYNAL, L. 1997 Instabilité et entrainement à l'interface d'une couche de mélange liquide–gaz. PhD thesis, Université Joseph Fourier Grenoble I.

RAYNAL, L., VILLERMAUX, E., LASHERAS, J.C. & HOPFINGER, E.J. 1997 Primary instability in liquid–gas shear layers. In *11th Symposium on Turbulent Shear Flows*.

SANCHIS, A. & JENSEN, A. 2011 Dynamic masking of PIV images using radon transform in free surface flows. *Exp. Fluids* **51**, 871–880.

SCARANO, F. & RIETHMULLER, M.L. 2000 Advances in iterative multigrid PIV image processing. *Exp. Fluids* **29** (7), S051–S060.

TILLETT, J.P.K. 1968 On the laminar flow in a free jet of liquid at high Reynolds numbers. *J. Fluid Mech.* **32** (2), 273–292.

VENTURI, D. & KARNIADAKIS, G. 2004 Gappy data and reconstruction procedures for flow past a cylinder. *J. Fluid Mech.* **519**, 315–336.

WESTERWEEL, J. & SCARANO, F. 2005 Universal outlier detection for PIV data. *Exp. Fluids* **39** (6), 1096–1100.

YECKO, P., ZALESKI, S. & FULLANA, J.M. 2005 Viscous modes in two-phase mixing layers. *Phys. Fluids* **14** (12), 4115–4122.